Temporal Clonal Tracing Reveals Tumor-Intrinsic IFNγ-Dependencies Driving Niche Adaptation and Early Metastatic Colonization

Emilija Aleksandrovic[1,3], Shaneann R. Fross[1,3], Samantha M. Golomb[1,3], Xiyu Liu[1,3], Zhuo Zhao[2,3], Nikitha M. Das[1,3], Tanner C. Reese[1,3], Wei Ma[1,3], Jacqueline Lopez[4], Zhenyu Zhong[3,7], Min Zhao[1,3], M. Sharon Stack[5,6], Siyuan Zhang[1, 3]

Affiliations:

1. Department of Pathology, UT Southwestern Medical Center, Dallas, TX, 75390, USA
2. Lyda Hill Department of Bioinformatics, School of Public Health, UT Southwestern Medical Center, Dallas, TX, 75390, USA
3. Harold C. Simmons Comprehensive Cancer Center, Dallas, TX, 75390, USA
4. Department of Biological Sciences, College of Science, University of Notre Dame, Notre Dame, IN 46556, USA
5. Department of Chemistry and Biochemistry, University of Notre Dame, Notre Dame, IN 46556, USA
6. Mike and Josie Harper Cancer Research Institute, University of Notre Dame, 1234 N. Notre Dame Avenue, South Bend, IN 46617, USA
7. Department of Immunology, UT Southwestern Medical Center, Dallas, TX, 75390, USA

*** Correspondence to:** Siyuan Zhang, M.D., Ph.D., Department of Pathology, UT Southwestern Medical Center, ND6.200A, 6001 Forest Park Rd., Dallas, TX 75235. E-mail: Siyuan.Zhang@UTSouthwestern.edu; Telephone: 214-648-6537

Key Words: Metastasis, Disseminating Tumor Cells (DTCs), Clonal dynamics, Metastatic niches, IFN-gamma (IFNγ), Anoikis, Single-cell RNA sequencing, MetTag barcoding, Lineage tracing, In vivo CRISPR Screen.

SUMMARY

Metastasis is an emergent continuum, driven by evolving reciprocal adaptations between continuously disseminating tumor cells (DTCs) and the specialized metastatic niches of distant organs. The interplay between intrinsic and niche-driven mechanisms that enables DTCs to survive and home to distant organs remains incompletely understood. Here, using MetTag, a single-cell barcoding and transcriptome profiling approach with time-stamped batch identifiers (BC.IDs) and functional CRISPR screening, we resolved the clonality, temporal dynamics, and molecular determinates of DTC colonization success across evolving metastatic niches. Deep sequencing of barcodes revealed preferred enrichment of early-disseminated clones across metastatic niches. Single-cell RNA sequencing (scRNA-seq) coupled with RNA velocity analyses in ascites and metastasis-bearing omenta uncovered an emergent and distinct interferon-gamma (IFNγ) centric transcriptional trajectory, enriched among early seeding clones. *In vivo* CRISPR/Cas9 screening of metastatic niche-specific signatures demonstrated that genes belonging to the IFNγ response are functionally important for peritoneal metastasis. Knockout of IFNγ receptor 1 (*Ifngr1*) in the first batch of DTCs significantly reduced metastatic burden and extended survival, underscoring the importance of tumor cell intrinsic IFNγ signaling in shaping post-seeding metastatic niche (PSMN) and subsequent metastatic co-evolution. Mechanistically, tumor intrinsic IFNγ response and ascites-derived tumor-associated macrophages (TAMs) protect cancer cells from anoikis-mediated death by promoting pro-survival signaling. Our study defines temporal dynamics of disseminating tumor cells at metastatic niches and reveals a general “first come, first served” pro-metastatic adaptation principle of DTCs.

INTRODUCTION

Cancer metastasis encompasses continuous metastatic dissemination from the primary tumor, followed by passive clonal selection, and active epigenetic niche adaptation in response to the metastatic niche[1]. Resolving the clonal, temporal, and microenvironmental determinants along the cancer metastatic continuum has long been a challenge in the field. Unlike most cancer types, where hematogenous metastasis

predominates, high-grade serous ovarian carcinoma (HGSOC) exhibits a unique pattern of transcoelomic, continuous local spreading within the peritoneal cavity, representing a metastatic continuum[2]. In HGSOC, malignant ascites functions as a “reservoir” of floating cancer cells and cell clusters – DTCs detached from the primary tumor – initially seeding locally within the peritoneal cavity before disseminating to distant organs[3]. Different from immunologically cold solid tumors, malignant ovarian cancer ascites is heavily enriched with immune cells and acellular factors known to influence tumor progression. Consequently, ovarian cancer DTCs - continuously shed from the primary tumor - must overcome immune surveillance and adapt to the unique intraperitoneal microenvironment to establish colonization[4,5,6,7]. Notably, initial and subsequent DTC colonization is not merely a passive adhesion to a distant organ, but an active remodeling of the surrounding microenvironment, leading to a consistently evolving post-seeding metastatic niche (PSMN) – a concept analogous to the pre-metastatic niche. However, the underlying molecular determinants that modulate reciprocal interplay between DTC seeding waves and PSMN evolution and drive the ultimate metastasis outgrowth remains largely unknown.

Here, we conducted comprehensive lineage tracing, single-cell RNA sequencing (scRNA-seq), *in vivo* CRISPR screening, and Cre-based niche-tracing analysis to dissect the complex interplay between continuously arriving DTCs and PSMN. We identified that early DTCs in ascites are dependent on anti-apoptotic niche-adaptive IFNγ response genes for omental colonization. Additionally, the interferon-rich ascites microenvironment harbors a macrophage population capable of protecting cancer cells from anoikis-mediated death via paracrine signaling. Together, our data provide novel insights into the temporal dynamics of ovarian cancer clonal dynamics and highlight ascites-specific factors that prime cancer cells for successful metastatic colonization.

RESULTS

MetTag Captures Clonal Lineage Across Metastatic Sites and Across Time

To capture the transcriptional dynamics across ovarian cancer metastasis, we created a “MetTag” tracing system by employing RNA-level barcoding based on the LARRY

92 (Lineage And RNA Recovery) barcoding construct, enabling single cell transcriptome-
93 level lineage tracing[8]. Importantly, we added a unique batch identifier “BC.ID” as a time
94 stamp for distinguishing time points (TP) of early or later-arriving DTCs. Within the U6-
95 driven MetTag sequence, a Chromium 10x capture sequence 1 (CS1) allows for
96 simultaneous capture of the MetTag transcript with mRNA transcripts (**Fig.1A, S1A-D**).
97 Diversity of each BC.ID library batch was confirmed by deep next-generation
98 sequencing (NGS). We observed a relatively consistent diversity across the six BC.ID
99 library batches comparable with the original depositor LARRY library (**Fig.S1B-D**).
100
101 Next, we generated six unique isogenic ID8 p53$^{-/-}$ murine ovarian cancer pools (BC.ID1-
102 6) with MetTag-GFP lentiviral libraries harboring BC.IDs (**Fig.1A**). To model the
103 continuous dissemination, individually LARRY barcoded (BC) and BC.ID batch-coded
104 cells were injected interperitoneally (i.p.) in a fractionated manner at low doses across
105 six different time points to model early, mid, and late waves of DTCs. Early DTCs refer
106 to the first two BC.ID batches and late DTCs represent the last two DTC batches
107 (**Fig.1B**). Four weeks after the final DTC exposure, ascitic fluid (Asc), omenta (Om), and
108 peritoneal fat pads (FPs) were extracted. This experimental scheme was performed
109 under several immune cell depletion conditions, including wild type C57BL/6J (WT)
110 mice, immunocompromised NOD.Cg-Rag1^{tm1Mom}IL2rg^{tm1Wjl}/SzJ (NRG) mice (lacking
111 functional T, B, and NK cells), and under conditions of macrophage (MAC) depletion via
112 chlodrosome administration. Temporally spaced DTC exposure resulted in robust
113 metastasis formation in fully immunocompetent mice, evidenced by ascites
114 accumulation and positive GFP signal in the omentum and peritoneal adipose tissue
115 (**Fig.S1E top**). Quantification of overall metastases burden in a separate cohort of ID8-
116 Luciferase injected mice indicated that lacking T, B, and NK cells lead to clearer ascites
117 and reduced omental weight (**Fig.S1E-F**). Moreover, chlodrosome-mediated
118 macrophage depletion in C57B6 mice resulted in reduced intraperitoneal metastases
119 burden under the fractionated injection schema (**Fig.S1G-H**), suggesting the potential
120 role of myeloid cell in ovarian cancer metastasis.
121

122 To dissect the relative contribution of each batch of DTCs continuous seeded at
123 intraperitoneal metastatic niches, we used MetTag amplicon DNA sequencing to
124 quantify the relative abundance of BC.IDs in final overt metastases: early timepoint
125 (*TP-1, TP-2*), mid (*TP-3, TP-4*), and late (*TP-5, TP-6*) arrivers (**Fig. 1B**, pie chart).
126 Interestingly, in the overt metastases collected from three distinct peritoneal niches
127 (omentum, ascites, and fat pad), we observed a consistent pattern of enrichment of
128 early BC.IDs, suggesting dominance of early arrivers in contributing to final metastasis
129 outcomes. Interestingly, we observed a near identical BC.ID distribution across all three
130 anatomical locations in both wild type and NRG mice (**Fig.1C-1E**), as well as
131 macrophage depleted host in omenta (**Fig.1C**), suggesting a negligible role of niche-
132 specific tumor immune microenvironment (TIME) in the overall dominance of early
133 arriving DTCs. To examine if later-arriving cancer cells are dispensable for overall
134 metastases burden, we evaluated tumor burden in mice with a single injection of tumor
135 cells (TP-1 only) compared to mice with fractionated dosing (TP1-6) as described in
136 Fig.1B in WT mice with luciferase-tagged ID8 p53$^{-/-}$ cells. At the experimental endpoint
137 of four weeks post final cancer cell injection, tumor burden levels were comparable
138 (**Fig.1F-G**), as measured by *in vivo* bioluminescent imaging (BLI). This data indicates
139 that early DTCs are not dependent on later DTCs for metastatic colonization and
140 outgrowth. Given the isogenic nature of disseminating ID8 p53-/- cancer cells and their
141 consistent genomic alterations, these results strongly suggest that early DTC
142 colonization reciprocally reshapes the PSMN, creating a less favorable tissue
143 environment for subsequent metastatic seeding.
144
145 To gain a better understanding of the transcriptional programs necessary for early DTCs
146 to colonize and subsequently assess their clonal expansion status, we performed CITE-
147 seq (scRNA-seq with HTO sample multiplexing) coupled with direct capture of U6-driven
148 MetTag transcripts via capture sequence 1 (CS1) (**Fig. 1H**). Sequential injections were
149 performed in the same manner as in Fig.1B with a reverse barcode injection schema to
150 ensure no unintended bias towards certain BC.IDs gained over the cell selection period.
151 Single cell analysis of MetTag BC.IDs of metastasis-bearing tissues revealed that early
152 DTCs (*TP1-2*) were enriched in overt metastases (**Fig.1I & 1J**). The prominent trend

153 towards early DTC dominance, especially in ascites (**Fig.1J**), was consistent with gDNA
154 sequencing data in Fig. 1C and 1D.
155
156 We next asked whether the dominance of early DTCs in overt metastases represents a
157 widespread niche-adaptive and PSMN conditioning feature of DTCs. We applied three
158 MetTag-BC.IDs in a triple negative breast cancer (TNBC) mouse model of lung
159 metastasis (Lung.Met): BC.ID1 representing early TP-1 and TP2, BC.ID2 representing
160 mid TP-3 and TP4, and BC.ID6 representing the late TP-5 and TP-6. In this model, we
161 identified almost exclusively early TP DTCs dominance (91.9%) in the overt lung
162 metastases, on the scRNA-seq level at experimental endpoint (**Fig. 1K**). Collectively,
163 this data suggests that early dissemination occurs in both hematogenous (TNBC) and
164 transcoelomic (ovarian) metastases.
165
166 **Clonal Transcriptomics Analysis of DTCs Reveals Shared Evolutionary Path**
167 **Towards Inflammatory Signature**
168 To further investigate characteristics of early and later arrived DTCs, we assessed
169 clonal dynamics in different metastatic niches. Specifically, as most DTCs do not survive
170 and only rare clones successfully adapt to metastatic niches[9], we examined whether
171 tumor cells disseminated over time evolve along diverse trajectories or converge on a
172 common path characterized by a limited set of adaptive transcriptome features. We first
173 integrated LARRY clonal barcode information with transcriptional profiles across ascites
174 and omental niches, followed by cell cluster annotation. We defined cells with high
175 levels of keratins and absence of CD45 transcript expression (*Krt18*+, *Krt8*+, *Ptprc*-) as
176 the tumor cell-enriched cluster on the UMAP (**Fig. 2A and S2A**). After reclustering
177 *Krt18*+/*Krt8*+/*Ptprc*- cells, cell cluster states were determined through a combination of
178 cluster marker genes and pathway-level analysis using the Escape R package[10] (**Fig.**
179 **S2B-E**). Ascites-derived cancer cells (AscMet) displayed distinct transcriptional states
180 from those in the omentum (OmMet) (**Fig. 2B-D**). Single Cell Gene Set Enrichment
181 Analysis (ssGSEA) further showed that ascites-derived cells were strongly enriched for
182 interferon alpha (IFNα) and gamma (IFNγ) signaling (cluster 3), as opposed to more
183 heterogeneous four distinct subclusters/modules in OmMet including proliferative,

184 epithelial-mesenchymal transitioning (EMT), matrisome, and a hypoxic, inflammatory
185 subclusters (**Fig. 2D & 2E**).
186
187 Cellular barcoding approaches have been widely used to reveal clonal dynamics driven
188 by both genetic predisposition and epigenetic changes in response to environmental
189 cues[11]. We asked whether the most expanded clones would 1) cluster together based
190 on transcriptional status, indicating strong genetically pre-determined cell-autonomous
191 programs driving metastasis, or 2) disperse into heterogeneous transcriptional states
192 (clusters) reflective of diverse transcriptional adaptation to different metastatic niche
193 cues (**Fig. 2F**). Interestingly, we observed minimal overlap between dominant
194 outgrowing clones across each HTO/mouse in both anatomical locations (**Fig. 2G**).
195 While one clone, BC-1, was shared across ascites and omenta, most of the highly
196 expanded clones are distinct between metastatic niches. These results suggest that
197 successful clonal outgrowth requires unique adaptations reflective of the specific
198 microenvironment.
199
200 Given that omentum metastases showed diverse single-cell transcriptional states (**Fig.**
201 **2D-E**), we projected clonal identity of the top expanded clones from omenta onto the
202 cancer cell UMAP and examined similarities between clones. At both the transcriptome
203 cluster and pathway levels, dominant clones were enriched for several defined
204 signatures (**Fig. 2H-2I, S2F**). Apart from the proliferative subcluster 4, expanded clones
205 consistently occupied the hypoxic, inflammatory subcluster 0 (**Fig. 2I**), suggesting
206 diverse, yet directed evolutionary trajectories within the same clonal lineage. To
207 understand the lineage relationships among different subclusters, we applied RNA
208 velocity and pseudotime analysis using scVelo and CellRank[12]. Paga velocity and
209 pseudotime analyses revealed a clear trajectory originating from the IFN signaling
210 enriched ascites compartment subcluster 3, leading to proliferative status, then further
211 converging to subcluster 0, a terminal inflammatory state in the omentum (**Fig. 2J & 2K,**
212 **Fig. S2G** top). Notably, IFNγ, but not the IFNα signature, was significantly enriched in
213 early DTCs (TP-1) (**Fig. 2L, S2G** bottom).

214 Similarly to our ovarian cancer dataset, we observed heterogeneous clonal distribution
215 between each mouse in the TNBC Lung.Met MetTag scRNA-seq dataset, suggesting
216 non-genetic, transcriptomic drivers of successful colonization (**Fig. S2H-S2I**). To
217 examine the generality of the enriched IFN signature in metastases, we performed a
218 separate scRNA-seq experiment comparing TNBC Lung.Met and in vitro cell culture
219 (**Fig. S3A**). scRNA-seq analyses revealed that, compared to cultured cells, *in vivo*
220 Lung.Met tumor expressed higher IFNγ and IFNα signatures (**Fig. S3B-S3E**).
221 Collectively, the ovarian and lung metastasis data suggests that transcriptional
222 adaptation towards IFN-signaling *in vivo* is a common trait of successfully colonized
223 DTCs. In ovarian metastasis specifically, successful metastatic clones in the omentum
224 occupy heterogeneous transcriptional states. These evolved phenotypes originate from
225 the ascites compartment, which encompasses an IFN-signaling-rich module that may
226 prime these later adaptations.
227
228 ***In vivo* CRISPR screen identifies functional essentiality of IFNγ signaling in**
229 **omental colonization**
230 As ovarian cancer cells initially disseminate into the peritoneal cavity, we next asked
231 whether transcriptional adaptation of cancer cells to the ascites environment is essential
232 for subsequent intraperitoneal seeding and successful omental metastasis. We
233 hypothesized that the ascites gene signature adopted by early DTCs – characterized by
234 limited nutrient availability and low attachment – is (1) induced by initial detachment
235 from a primary tumor and (2) necessary for subsequent peritoneal metastasis. To test
236 this hypothesis, we performed differential gene expression (DEG) analysis and over-
237 representation pathway analysis (ORA) with clusterProfiler[13] to compare gene
238 expression in metastatic tumor cells residing in the two distinct niche compartments
239 (Asc vs Om). Compared to OmMet, DEGs of AscMet were enriched in hemoglobin
240 genes (*Hbb-bs, Hba-a1, Hba-a2, Hbb-bt*) and interferon-stimulated genes (*Ifi27l2a* and
241 *Irf7*). In contrast, OmMets were enriched in immediate-early response genes (*Atf3,*
242 *Egr1, Fos, Fosb, Jun*)[14,15], adaptive immune immunoglobulin components (*Igkc, Igha,*
243 *Jchain*)[16], and angiogenesis (*Vegfa*) (**Fig. 3A**). Next, IFNγ/IFNα module scoring and
244 pathway analysis further highlighted a dominant interferon-rich inflammatory signature

245 in AscMet, as opposed to more heterogeneous programs in OmMet (**Fig. 3B, Fig. S3F-**
246 **S3H**).
247
248 To assess the functional significance of AscMet-OmMet DEGs, we designed a custom *in*
249 *vivo* CRISPR/Cas9 screen targeting 100 DEGs identified (**Fig. 3C,** "In Vivo Ovarian
250 Metastatic Niche Signature Screen"). SpCas9 was introduced into ID8 p53$^{-/-}$ cancer
251 cells and validated (**Fig. S3I & S3J**). 2.4 million cells (~2000X representation of sgRNA
252 library) were i.p. injected to a whole-body Cas9-expressing host (**Fig. 3C**). This host has
253 central tolerance to Cas9, decreasing immunogenicity towards Cas9-expressing tumor
254 cells[17]. Six weeks post-injection, metastasis-bearing omenta and ascites were
255 harvested for gRNA target amplicon sequencing and analysis (**Fig. 3C**)[18]. The positive
256 controls for the screen, *Pten* gRNAs, were significantly enriched in metastases derived
257 from both anatomical locations (**Fig. 3D & 3E**). Compared to the initial injected cell pool
258 sgRNA distribution, sgRNAs targeting eight genes in OmMet and ten genes in AscMet
259 were significantly depleted ($p < 0.05$) (**Fig. 3D-E**). The top depleted (dropout) genes –
260 *CD300lb*, *Ms4a8a*, *Marco*, *Gbp2b* (OmMet), and *Slfn1* (AscMet) – were "upregulated"
261 DEGs associated with AscMet, suggesting a necessity of initial transcriptome adaptation
262 to the ascites niche - the first niche DTCs encounter - for subsequent metastasis.
263 Furthermore, GSEA analysis of dropout genes using the GO Biological Function
264 (GOBP) gene sets revealed a shared enrichment of apoptotic cell clearance processes
265 in both Asc and Om compartments and enrichment of programs related to IFNγ in
266 omentum (**Fig. 3F**). To experimentally validate whether IFNγ is required for the
267 transcriptional upregulation of CRISPR screen hits in cancer cells, we treated ID8 p53$^{-/-}$
268 cells *in vitro* with recombinant IFNγ. We tested the inducibility of *Marco*, *Gbp2b*, and
269 *Slfn1* by IFNγ via RT-qPCR, where *Stat1* and *Irf1* transcription factors served as positive
270 controls for IFNγ response[19] (**Fig. 3G**). By 24 hours of treatment, all three genes were
271 significantly induced by IFNγ (**Fig. 3G**). The protein level of Gbp2b, an interferon-
272 inducible GTPase, was also significantly induced by IFNγ (**Fig. 3H**). Collectively, despite
273 the transcriptional heterogeneity revealed by scRNA-seq, consistent enrichment of
274 apoptotic pathway and the sequential activation of an IFNγ response (first in ascites,

275 then required for omental metastasis) suggest two functionally essential adaptive
276 mechanisms employed by DTCs to survive.
277
278 **Loss of IFNγ response in DTCs significantly decreases peritoneal metastases and**
279 **extends overall survival**
280 Because the top hits from our CRISPR screen are IFNγ-inducible genes, we
281 hypothesized that IFNγ may function as a primary regulator that exerts broader pro-
282 metastatic adaptive cellular programs in DTCs. Thus, instead of focusing on a single
283 downstream gene target, we sought to disable the entire cascade via IFNG receptor 1
284 knockout. We first confirmed robust expression of IFNγ receptor 1, *Ifngr1,* in both
285 AscMet and OmMet in vivo (**Fig. S3K**). Next, we genetically knocked out *Ifngr1* in ID8
286 $p53^{-/-}$ cells. Successful knockout of *Ifngr1* was validated via flow cytometry (**Fig. S3L**)
287 and ablation of the IFNγ transcriptional downstream targets was validated via western
288 blot probing for Stat1 and Gbp2b (**Fig. S3M**). We next i.p. injected ID8.Luciferase-
289 sgNTC or ID8.Luciferase-sgIfngr1 to Cas9-expressing mice. Tumor burden was
290 monitored by BLI intensity throughout the 6-week experimental window (**Fig. 3I**).
291 sgIfngr1 groups showed a significant reduction of overall metastasis burden compared
292 with sgNTC group (**Fig. 3J, Fig. S3N**). In contrast to sgNTC group, ~80% of mice in the
293 sgIfngr1 group remained alive at the end of the survival study ($p = 0.004$) (**Fig. 3K**). This
294 notion is consistent with the observation in human ovarian cancer microarray gene
295 expression data[20]. Patients with ovarian cancer expressing lower levels of *IFNGR1*
296 exhibited longer progression-free survival compared to the higher expressing group
297 (**Fig. S3O**).
298
299 Above results demonstrated that DTCs' intrinsic IFNγ signaling is essential for the
300 overall metastatic outcome. Given early DTCs (TP-1) showed a significantly higher IFNγ
301 signaling comparing with later DTCs (**Fig. 2L**), we next investigated whether the IFNγ
302 response in early DTCs influences the success of subsequent waves of DTC
303 colonization. We specifically perturbed IFNγ response (sgIfngr1) in the first batch of
304 early DTCs (G2), but not the immediate second wave of DTCs (sgNTC2) (**Fig. 3L**).
305 Interestingly, loss of Ifngr1 in the first batch of DTCs significantly reduced overall

306 metastasis burden at the endpoint (**Fig. 3M**). In the residual metastases in the sgIfngr1
307 group (G2), control (sgNTC2) cells outcompete the sgIfngr1 cells, as quantified through
308 sgRNA amplicon sequencing (**Fig. 3N**). Taken together, these results demonstrated that
309 (1) a robust IFNγ response in the initial seeded DTCs prevent the colonization of later
310 DTCs - potentially through conditioning of PSMN - and (2) are paradoxically required for
311 overall metastasis success.
312
313 **IFNγ response mediates resistance to anoikis by activating pro-survival programs**
314 We next sought to examine mechanisms by which IFNγ signaling promotes metastasis.
315 First, we observed that *Ifngr1* knockout did not alter cancer cell fitness under standard
316 adherent culture conditions in the presence or absence of IFNγ treatment, evidenced by
317 both CellTiter-Glo luminescent cell viability assay (**Fig. 4A**, left) and colony count
318 formation (**Fig. S4A**). Interestingly, IFNγ treatment had a protective effect and increased
319 cell viability in control (sgNTC) cells under ultra-low attachment (ULA) conditions. This
320 protective effect was ablated in the *sgIfngr1* group (**Fig. 4A**, right).
321
322 To investigate the mechanism underlying increased cancer cell survival under IFNγ
323 treatment and ULA conditions, we performed bulk RNA-seq (**Fig. S4B**) with wild type
324 (sgNTC) and single clone knockout line (sgIfngr1). First, principal component analysis
325 (PCA) and MA dispersion plot showed that ULA culture alone induced significant
326 transcriptomic shifts in both sgNTC and sgIfngr1 cells (**Fig. S4C-D**). ULA culture
327 condition induced pathways associated with TGFβ and platelet functions in sgNTC cells
328 **(Fig. S4E)**. sgNTC cells that survived under ULA conditions showed an overall reduced
329 S/G2 signature (**Fig. S4F**). Next, we compared the transcriptomic changes in response
330 to IFNγ. PCA of all groups revealed variance between sgNTC cells treated with PBS and
331 IFNγ (**Fig. S4C**). This IFNγ induced variance was ablated in the sgIfngr1 (KO) line as
332 expected, independent of culture conditions (**Fig. S4C**). We analyzed differentially
333 expressed genes (DEGs) between cells with or without IFNγ treatment under both
334 regular and ULA conditions (**Fig. 4B**). Interestingly, despite lower proliferation, cells
335 grown under ULA condition exhibited transcriptionally diverse responses (**Fig. 4B**) and

336 were overall more responsive to IFNγ than under regular condition, rendering more
337 DEGs detected (**Fig. 4C and S4C**). Besides 25 common IFNγ responsive genes, we
338 discovered 30 IFNγ responsive genes uniquely up-regulated only under ULA condition
339 (**Fig. 4C & S4G**). We next grouped the unique 30 upregulated genes into broad classes.
340 As expected, most genes represented classical interferon stimulated genes (ISGs) with
341 known roles in viral defense and antigen presentation (**Fig. 4D**). In addition, we
342 discovered several non-canonical ISGs, such as the immunoproteasome 20S subunit
343 beta 10 (*Psmb10*), poly(ADP-ribose) polymerase family member 14 (*Parp14*), as well as
344 PD-L1 (*Cd274*), in response to IFNγ under ULA condition (**Fig. 4D**). Both the canonical
345 and non-canonical ISG signatures were reflected in pathway analysis where the most
346 significant Reactome pathways were related to antigen processing and presentation, as
347 well as proteasome assembly and endosomal trafficking (**Fig. 4E**). Importantly,
348 Psmb10, Parp14, and PD-L1 all have reported context dependent, cell autonomous pro-
349 survival functions[21–24]. Indeed, knocking out IFNGR1 downstream *Stat1* and *Irf1* ablated
350 IFN downstream signaling (**Fig. S4H**) and led to a loss of IFNγ-induced pro-survival
351 phenotype under ULA (**Fig. 4F-G**).
352
353 To validate *in vivo* relevance of our findings, we analyzed above DEGs detected in bulk
354 RNA-seq using our single cell RNA-seq data derived from ovarian metastases. *In vivo*
355 AscMet exhibited higher levels of immunoproteasome genes (*Psmb10*, *Psmb9*) as well
356 as poly(ADP-ribose) polymerase family members (*Parp12*, *Parp14*, and *Parp9*)
357 compared with OmMet (**Fig. 4H**). Unexpectedly, *Cd274* was more highly expressed in
358 OmMet (**Fig. 4H**). Next, we performed RNA-based gating and defined *Irf1*^{high} and *Irf1*^{low}
359 cancer cells to represent IFNγ downstream responsive levels of each cell (**Fig. 4I)**.
360 *Irf1*^{high} cells upregulated *Parp14*, but not *Cd274* and *Psmb10* (**Fig. 4J**). Parp14 is known
361 to inhibit apoptosis by regulating Jun N-terminal kinase 1 (JNK1) in multiple myeloma[23].
362 Moreover, in ovarian cancer microarray data, low PARP14 expression correlates with
363 prolonged progression free survival, particularly at earlier primary tumor stages (**Fig.
364 S4I**).
365
366 **Myeloid cells are the major interacting partners to tumor cells**

367 In ascites, DTC's IFNγ response under low attachment condition is likely influenced by
368 the crosstalk with ascites niche-specific cells. To identify IFNγ producers and responders
369 within the ovarian metastatic niche, we first examined the expression patterns of
370 IFNγ and IFN-responsive genes identified in our CRISPR screen across all cells
371 detected in our MetTag single cell dataset (**Fig. 5A, S5A & S5B**). While T/NK cell
372 populations are the main producers of IFNγ, a significant proportion of myeloid cells
373 expressed a high level of CRISPR hits detected in tumor cells (*Gbp2b*, *Marco*, *Ms4a8a*,
374 *CD300lb*, and *Slfn1*) (**Fig. 5A**), suggesting myeloid cell similarly respond to available
375 IFNγ in the metastatic niche.
376
377 CellChat[25] analysis identified a significant increase in both the number and strength of
378 cell-cell interactions under OmMet condition compared with naïve condition (**Fig. S5C**).
379 Specifically, tumor cells primarily interacted with myeloid cells in both ascites in
380 omentum, while interactions with stromal cells were evident in the metastatic omentum
381 (**Fig. 5B**). These results suggest macrophages may be a key axis of communication that
382 shapes DTCs' response to both IFNγ and detachment conditions in ascites. Focusing on
383 the myeloid compartment, we grouped Seurat clusters into broader cell identity
384 categories (**Fig. S5A-B**) and found a proportional increase of myeloid cells in both
385 metastatic sites compared to their naïve counterparts (**Fig. 5C**). Subclustering the
386 myeloid population revealed that the major contribution to the proportional increase are
387 subclusters 0,1, 5, and 6 (**Fig. 5D, Fig. S5D**). Those highly heterogenous macrophage
388 subclusters expressed diverse tumor-associated macrophage (TAM) markers, such as
389 *Adgre1*, *Cd68*, *Csf1r*, *Itgam*, *Mertk*, and *Trem2* (**Fig. S5E**). RNA velocity analysis
390 revealed a dynamic transition from the ascites-derived myeloid clusters 1 and 5 toward
391 omental-specific myeloid clusters 0 and 6 (**Fig. 5E**). Omental clusters 0 and 6 were
392 characterized by increased expression of costimulatory molecules and angiogenesis
393 genes as compared to ascites clusters 1 and 5 (**Fig. 5F, Fig. S5F**). Collectively, the RNA
394 velocity and DEG analyses suggest that ascites-derived TAMs may represent a less
395 differentiated state relative to omental TAMs.
396

397 Given the apparent macrophage niche-dependent differentiation states, we next asked
398 whether omental TAMs reflect a polarized, terminal state within the metastatic niche. If
399 so, increased TAM polarization would likely shape the T cell compartment[26,27]. Indeed,
400 while the ascites-derived T/NK compartment was dominated by a mixture of naïve
401 CD4+ and CD8 +T cells, omental metastases and niche tissue contained a broader and
402 more complex repertoire of activated, exhausted, and regulatory T cells (**Fig. 5G**)
403 enriched in pathways related to regulation of immune cell activation (**Fig. S5G**). We next
404 subsetted macrophages (*Cd68*^{high}/*Adgre1*^{high}, **Fig. S5H**) and scored them against M1
405 and M2 gene modules. Compared to ascites-derived TAMs, omental TAMs exhibited
406 higher hybrid functional state scores (**Fig. S5I**), reflecting an immunomodulatory TAM
407 cellular state[28] that cannot be captured by binning into a strictly immune-promoting or
408 suppressing category. Unlike the immunomodulatory and ECM-related omental
409 signatures, ascites-derived TAMs were enriched in pathways associated with cellular
410 stress responses and NRF2-dependent redox metabolism (**Fig. 5H & 5I**). On the
411 individual gene expression level, ascites TAM signatures were reflected in elevated
412 expression of key stress-related genes – including *Anxa1* and *Hmox1* – as well as
413 *Ndufb8* and *Cox5a*, components of mitochondrial respiration (**Fig. S5J**). These findings
414 indicate that ascites TAMs may represent an earlier, less polarized yet metabolically
415 active state, while omental TAMs have transitioned into an immunomodulatory,
416 polarized phenotype. Finally, we utilized flow cytometry to validate immune cell
417 dynamics observed in the scRNA-seq dataset (**Fig. S5K**). GFP+ cancer cells were
418 detected in both metastases-bearing ascites and omental samples. While there was a
419 significant increase in CD11b+/CD11c+ macrophages as well as CD11b-/CD11c+ DCs
420 in ascites, metastatic omentum samples were significantly enriched in mature F4/80+
421 TAMs and cytotoxic CD8+ T cells (**Fig. S5K**). These findings further implicate the
422 omental environment in fostering a highly immunomodulatory population of TAMs.
423
424
425 **Peritoneal macrophages are direct DTC pro-survival interactors**
426 We first tested whether macrophages are functionally important in promoting ovarian
427 cancer metastasis. Macrophage depletion via direct i.p. liposomal chlodronate injections

428 (**Fig. 6A**) demonstrated that peritoneal TAMs are pro-metastatic: depleting TAMs
429 significantly reduced omental weights and CD45 negative cancer cell frequencies in
430 ascites at experimental endpoint (**Fig. 6A**, **Fig. SAB** flow gating strategy and depletion
431 validation). Although TAM-induced immunomodulation is a well-established metastasis
432 driver, less is known about the role of direct TAM-tumor cell interactions in ovarian
433 cancer metastasis. To identify cells that are in close contact or has been contacted with
434 ovarian metastases, we developed a non-SP-TATK Cre-based iteration of the
435 "NicheTracing" system to genetically trace microenvironmental contacts *in vivo* over a
436 prolonged timeframe. In this system, cancer cells expressing Cre.ERT2 were injected
437 into Ai6 (RCL-zsGreen) Cre reporter mice. Upon intercellular-cytoplasmic transfer and
438 Tamoxifen-mediated nuclear entry of Cre into neighboring cells, Cre-mediated
439 recombination turns on the zsGreen cassette in host cells (**Fig. 6B**). After validating
440 Cre.ERT2 expression in transduced cell lines (**Fig. S6A**), we benchmarked this system
441 using *in vitro* coculture (**Fig. S6B-S6F**) and in an independent model of TNBC lung
442 metastasis established using the E0771 cell line (**Fig. S6G-H**). In the ovarian metastasis
443 model, we readily detected zsGreen+ (ZsG) niche cells in both metastasis-bearing
444 omenta and ascites at the experimental endpoint six weeks post cancer cell injection
445 (**Fig. 6B**). We performed flow cytometry analysis on ascites and gated cells into ZsG^{low}
446 and ZsG^{high} (**Fig. 6C**). Unlike ZsG cells detected in lung metastases where only ~30%
447 ZsG^{high} cells were $F4/80^{+}$ macrophages (**Fig. S6H**, right panel), over 90% of ZsG^{high}
448 host cells were $F4/80^{+}/Ly6G^{low}$ TAMs (**Fig. 6C**).
449
450 Interestingly, a significant portion of ZsG^{high} $F4/80^{+}/Ly6G^{low}$ TAMs expressed a specific
451 macrophage marker Trem2 (**Fig. 6D, Fig. S6I-J**). To explore the transcriptome
452 differences between $Trem2^{high}$ and $Trem2^{low}$ myeloid cells, we specifically analyzed
453 those two groups of myeloid cells using our scRNA-seq dataset. $Trem2^{high}$ showed a
454 high expression of Olfml3, Tmem119, Mmmp13 genes, reflecting broad chemotaxis,
455 ERK pathway, and adhesion pathways (**Fig. 6E and Fig. S6L)**. In contrast, significantly
456 enriched pathways in $Trem2^{low}$ cell were related to epithelial cell proliferation,
457 mesenchymal transition, and TGFβ pathways (**Fig. S6L**), demonstrating distinct roles of
458 these macrophage subsets. As Trem2+ macrophages are known to play lipid sensing,

459 anti-inflammatory and immunosuppressive tumor promoting roles[29,30,31], we next
460 investigated the functional significance of Trem2 signaling in ovarian cancer metastasis.
461 After induction of experimental ovarian metastasis in macrophage-specific (Lyz2-driven)
462 Trem2 KO mice (**Fig. 6F and Fig. S6M**), unexpectedly, we observed no significant effect
463 of the Trem2 KO on ovarian metastasis burden (**Fig. S6M**). As ablating Trem2 signaling
464 in macrophages was not sufficient to change the overall ovarian cancer metastasis
465 progression, these data suggest that peritoneal macrophages, even Trem2 low subsets,
466 could promote metastasis independently from known Trem2-mediated efferocytotic and
467 anti-inflammatory programs.
468
469 We next explored whether peritoneal macrophages could promote cancer cell survival
470 under low attachment conditions. We performed a macrophage-cancer cell coculture
471 under ULA conditions. Macrophages from peritoneal lavage were enriched using F4/80
472 magnetic beads (**Fig. 6H**, **Fig. S7B & S7C** flow gating strategy) and cocultured with
473 three different murine ovarian cancer cell lines; ID8 p53$^{-/-}$, ID8 p53$^{-/-}$ BRCA2$^{-/-}$, and
474 PPNM[32] (**Fig. 6I, S7D** flow gating strategy). After a 48-hour coculture period, flow
475 cytometry analysis revealed that cancer cell viability, as measured by live/dead staining
476 (ZombieAqua), decreased under ULA conditions compared to regular attachment
477 plates. Most importantly, survival was partially rescued with macrophage coculture
478 across all three cell lines (**Fig. 6I**). These results indicate that peritoneal macrophages
479 directly support cancer cell survival under low attachment conditions.
480
481 **Patient and murine ascites-derived TAMs provide TNF to cancer cells**
482 To determine if tumor-supportive macrophage interactions occur in human ovarian
483 cancer, we analyzed a human-derived single-cell dataset containing over 200,000 single
484 cells from 14 ovarian cancer patients and collected from five locations: peripheral blood
485 (PB), peripheral lymph nodes (PLN), malignant ascites (Asc), primary tumor (Pri.OT),
486 and matched metastatic tumor (Met.Ome)[33]. As observed in our murine scRNA-seq
487 dataset, cancer cell-containing compartments, including Asc/Pri.OT/Met.Ome, had
488 increased proportions of macrophages compared to PB and PLN (**Fig. 6J & Fig. S8A**).
489 DEG analysis between TAMs at metastatic sites (**Fig. S8B**) and subsequent GO

490 pathway analysis conducted on the DEG list revealed immune-modulatory pathways
491 (cytokine, chemokine, allograft rejection) were upregulated in Om.TAMs while cargo
492 receptor activity related genes were enriched in As.TAMs (**Fig. S8C**).
493
494 Our macrophage-tumor co-culture assay (**Fig. 6H-I**) suggests that macrophages could
495 support tumor cell through macrophage-derived factors. Therefore, we applied NicheNet
496 analysis to further characterize ligand-receptor interactions between macrophage
497 (ligand provider) and tumor cells (signaling receiver through receptor) (**Fig. 6K**). We
498 implemented this strategy to both our murine dataset as well as the patient dataset (**Fig.**
499 **S8E**). After defining myeloid cells (Broad cell ID) as the sender cell type in the murine
500 dataset and macrophage cluster as the sender in the human dataset, we compared the
501 top predicted tumor-interacting ligands in each dataset. We found four overlapping
502 sender ligands across species - *TGFB1*, *IL10*, *TNF, and IL-1β*- that were the most
503 significant ligands predicted to interact with cancer cell receptors (**Fig. 6K, Fig. S8D-E**).
504 Notably, these ligands were detected at a high-level in patient macrophages (**Fig. S8F**).
505 Next, we examined the top predicted downstream target genes in cancer cells affected
506 by top TAM ligands. Pathway analysis of the predicted downstream genes yielded
507 pathways involved in cell-cell adhesion, response to oxygen levels, and apoptosis
508 regulation (**Fig. S8G**). For the common ligands (*TGFB1, IL10, TNF, and IL-1β*) we
509 derived a list of possible corresponding receptors (common receptors) based on "prior
510 interaction potential" in the NicheNet analysis. Interestingly, cross-examination of
511 corresponding common receptor expression in the bulk RNA-seq data derived from ULA
512 culture condition (**Fig 4**) showed that a subset for receptors were significantly up-
513 regulated in response to ULA culture condition (e.g. *Tgfbr1/2*, *Il1r1*, and *Il10rb*). Such
514 ULA-dependent receptor up-regulation was largely independent of IFNγ treatment (**Fig.**
515 **6L**). In parallel to cancer cell intrinsic IFNγ programs, these data suggest that ascites-
516 derived TAMs provide a cocktail of ligands that provide additional pro-survival signals to
517 IFNγ-primed AscMet cells to survive.
518
519 **DISCUSSION**
520

521 **Early DTC dominance phenotype in ovarian cancer metastasis**
522 DTC-niche interactions at each stage of the metastatic cascade fundamentally
523 determine disease progression and patient outcomes. Following the initial wave of
524 metastatic dissemination, early DTCs inevitably reshape the metastatic niche
525 microenvironment, irrespective of whether they ultimately survive or perish upon arrival.
526 The niche remodeling by pioneer DTCs likely exerts more profound effects on
527 subsequent colonization than distant signals from the primary tumor. While the pre-
528 metastatic niche (PMN) has been extensively characterized[34,35], this dynamic process
529 following DTC seeding creates what we term the Post-Seeding Metastatic Niche
530 (PSMN). The multi-cellular dynamics resulting from progressive DTC accumulation at
531 newly colonized PSMN mirrors a well-established ecological concept: the Allee effect,
532 which describes how population growth rates depend on population density through
533 competition or cooperation. Although the Allee effect has been demonstrated in
534 metastatic contexts using in vitro models[36], how continuously arriving DTCs dynamically
535 alter PSMN properties and influence the fate of later-arriving tumor cells within the intact
536 physiology of living systems remains unstudied.
537
538 Leveraging our MetTag barcoding and staggered injection model, the data presented
539 here consistently demonstrated a skewed overrepresentation of early disseminated
540 tumor cells (DTCs): TP-1 and TP-2 DTCs overwhelmingly dominate the metastatic
541 burden at day 40, whereas cells introduced at later days (TP-6) showed minimal
542 contributions to final overt metastases. This pattern persists across immunocompetent,
543 immunodeficient (NRG), and macrophage-depleted hosts, as well as TNBC lung
544 metastasis model (**Fig. 1**). This skewness in early DTC dominance cannot simply be
545 attributed to inherent, longer chronological growth times of early DTCs, as there
546 remains an ample growth window for TP-6 cells (from Day 11 to Day 40). Additionally,
547 these results are consistent with early cancer cell dissemination suggested by clinical
548 tumor genetics studies in ovarian and breast cancer metastasis[37–40]. There are several
549 non-mutually exclusive hypotheses that could explain early DTC dominance observed in
550 our study. First, the omentum might contain a limited number of permissive micro-niches
551 that favor DTC colonization. Pioneer DTCs might rapidly saturate these micro-niches

552 and monopolize spatial resources – a “first come, first served” model. Second, the
553 immune-independent nature of skewed distribution of temporally disseminated DTCs
554 suggests a role of non-immune stromal elements in dictating colonization success. Early
555 DTCs may actively remodel the niche, rendering it unfavorable for later DTCs.
556 Comprehensive spatiotemporally resolved imaging and genomics analyses are required
557 to further explore these hypotheses.
558
559 **Duality of IFNγ signaling-driven metastatic adaptation**
560 Beyond the “seed and soil” hypothesis, it has been increasingly appreciated that
561 metastasis is not merely passive fitness-based selection of DTC clones at the niche, but
562 also an active epigenetic DTC-niche mutual adaptation process. Our single-cell
563 transcriptome analysis, coupled with barcoding clonal analysis, provided us with clonal
564 resolution of the underlying genetic and epigenetic determinants governing DTC
565 behavior. Interestingly, instead of occupying unique transcriptome clusters - which
566 would likely suggest distinctive genetic mutational features - the expanded clones form
567 similar coordinated adaptive “mini-ecosystems” encompassing multifaceted
568 transcriptome features that converge toward an inflammatory/IFNγ response (**Fig. 2H-**
569 **L**). This data aligns with single-cell whole-genome sequencing (scWGS) of treatment
570 naïve ovarian cancer patients which details the existence of (1) significant clonal
571 heterogeneity within the same patient and (2) distinct IFNα/IFNγ expressing clones[54].
572 Our CRISPR/Cas9 *in vivo* screen results (**Fig. 3**) further support the notion that cancer
573 cell fitness in the peritoneal cavity and subsequent omental metastasis depend on rapid,
574 transcriptional-level adaptation to IFNγ-responsive programs. Intriguingly, our data
575 indicate that the early DTCs IFNγ response is required for subsequent metastatic
576 seeding (**Fig. 3L-N**). Knocking out IFNGR1 in the early batch of DTCs significantly
577 reduced the colonization success of later DTCs with intact IFNGR1, indicating a critical
578 temporal window in which early IFNγ responsiveness and active PSMN conditioning by
579 initial colonized DTCs jointly drive the subsequent metastatic continuum. Our findings
580 expand the conventional view of clonal fitness by revealing its temporal and niche-
581 dependent nature, where transient adaptive states at critical windows determine
582 metastatic success. In this “first come, first served” model, early metastatic DTC–niche

583 crosstalk through IFNγ sensing and epigenetic adaptation determines metastasis
584 success by enabling the earliest colonizers to occupy and remodel permissive micro-
585 niches while preventing later DTCs' entry.
586
587 Although the findings presented here support a tumor cell-centric pro-metastatic role of
588 IFNγ, it is important to note that IFNγ in metastatic niches can act in complex ways. In
589 some cancers, IFNγ reduces metastasis through activation of effector T and NK cells,
590 thereby enhancing the effectiveness of immunotherapy[41,42]. Furthermore, in some
591 contexts, IFNγ can induce apoptosis in regulatory T cells and inhibit angiogenesis[43].
592 Specifically in ovarian cancer cells, both anti-metastatic and pro-metastatic roles have
593 been reported[44,45]. IFNγ has been shown to synergize with beta glucan treatment to
594 reduce peritoneal metastasis and Ifngr1 knockout in host cells leading to a significant
595 increase in metastasis[46]. For pro-metastatic roles, IFNγ has been previously reported to
596 upregulate PD-L1 and IL-8 in ovarian cancer cells, leading to increased cell migration
597 and proliferation[45]. We did not observe any proliferation differences via colony formation
598 assay *in vitro* (**Fig. S4A**) after a 7-day IFNγ exposure. Given that PD-L1 and Psmb10
599 levels were not increased in Irf1^{high} cells *in vivo* (**Fig. 4J**), we nominate increased
600 *Parp14* as an active pro-survival cellular adaptation maintained in ascites over time, as
601 opposed to an immediate physiological response to IFNγ signaling. Based on the data
602 presented here, we believe that, although both effector immune cells and cancer cells
603 could be impacted by IFNγ, IFNγ response in cancer cells (intrinsically) leads to an
604 overall pro-metastatic effect. This effect is an important mechanism driving metastasis
605 and it should be carefully considered when designing anti-metastasis treatment.
606
607 **Macrophage plasticity and pro-survival ligands**
608 Cells of the myeloid lineage are characterized by significant plasticity, especially in
609 disease[47,48]. However, recent studies point to niche-regulated plasticity restriction[49].
610 Upon infiltration of inflammatory monocytes into metastatic sites, they often exhibit
611 "commonly described" reprogrammed states such as increased checkpoint expression
612 or efferocytotic receptor upregulation due to cancer cell engulfment. In addition to these
613 classical reprogramming events, myeloid cells exhibit tissue-specific reprogramming

614 after prolonged residence at a specific niche[49]. Thus, although we observe Trem2^{high}
615 macrophages in metastatic omenta and ascites, depleting Trem2 signaling in those cells
616 did not significantly impact on metastasis phenotype (**Fig. 6F-G**), pointing the role of
617 other programs within the broad myeloid population that could provide support to cancer
618 cells. Although IFNγ treatment is sufficient to trigger expression of anti-apoptotic genes
619 such as *Parp14*, and loss of attachment triggers *IL-1β*, *TNF*, *TGFβ*, and *IL10* receptor
620 transcription (**Fig. 6L**), our data suggests that macrophages provide multiple pro-
621 survival signals to primed cancer cells. Specifically, TNF itself[50] and *IL-1β*[51] are known
622 amplifiers of NF-kB, a master-regulator of anti-apoptotic and anti-necrotic gene
623 expression[52]. TGFβ has been reported to activate the pro-survival P3-k/Akt pathway in
624 certain contexts[53,54]. The cancer cell-intrinsic roles of IL10 warrant more investigation.
625 Given the known roles of TNF, *IL-1β*, and TGFβ and increased receptor expression in
626 cancer cells when cultured under ULA conditions, we hypothesize that initial
627 IFNγ exposure and loss of attachment may prime DTCs to respond strongly to
628 macrophage-derived pro-survival cues and collectively amplified pro-survival programs
629 in DTCs.
630
631 In summary, our study dissected the complex landscape of ovarian cancer metastasis
632 through a systematic characterization of both cancer cells and local immune factors
633 using MetTag temporal, clonal and scRNA-seq analysis. Our findings highlight the
634 importance of ascites as a functional reservoir for these factors and that early
635 acquisition of IFNγ response and interaction with macrophages are necessary
636 deterministic adaptation steps for DTCs to survive and colonize.
637
638 **ACKNOWLEDGMENTS**
639 This study was partially funded by the NIH T32GM075762 training grant (E. A.), NIH
640 R01 CA194697-01 (S.Z.), NIH R01 CA255064-01A1 (S.Z.), NIH R21 CA263798-01
641 (S.Z.), Cancer Prevention and Research Institute of Texas (CPRIT) Scholar Award
642 RR220024 (S.Z.), CPRIT Individual Investigator Research Awards RP230261
643 (Z.Zhong), and NIH R35GM142654 (Z.Zhong). We are additionally grateful to the Dee
644 Family endowment (S.Z.) and to the following core facilities: Notre Dame Freimann Life

Sciences Center, Notre Dame Genomics and Bioinformatics Core Facility, Indiana University School of Medicine Center for Medical Genomics, Indiana University Simon Cancer Center, Simmons Comprehensive Cancer Center, UT Southwestern (UTSW) Animal Resource Center, UTSW Flow Cytometry Core, and UTSW Small Animal Imaging Core Facility. The computational arm of this research project was, in part, supported by the BioHPC supercomputing facility at UTSW.

AUTHOR CONTRIBUTIONS

Conceptualization and experiment design, E.A., M.S.S. and S.Z.; Data analysis, E.A., S.Z., X.L., Z. Zhao; Experiments and methodology, E.A., S.Z., S.R.F., S.M.G., J.L., W.M., N.D., T.C.R., M.Z., Z. Zhong; Manuscript writing and revision, E.A., S.M.G., and S.Z.; Study supervision, S.Z. We attest that all coauthors reviewed and pre-approved the manuscript before submission.

DECLARATION OF INTERESTS

We do not have any competing interests to declare.

FIGURE LEGENDS

Figure 1: Tracking Clonal Lineage in Ovarian Cancer Metastasis

(**A**) Schematic depicting main elements of the MetTag library barcoding construct. (**B**) Schematic of injection and tissue collection timeline for the staggered injection experimental model using MetTag-barcoded ID8 ovarian cell lines. Schematic was partially created with BioRender.com. (**C**) Genomic DNA (gDNA)-level barcode distributions in the omentum graphed as frequency under WT, NRG, and MAC depletion conditions. (**D-E**) gDNA-level barcode distributions in ascites and pelvic fat pads under WT and NRG conditions. In (C-E) panels, BC.ID1 = TP-1, BC.ID2 = TP-2, BC.ID3 = TP-3, BC.ID4 = TP-4, BC.ID5 = TP-5, BC.ID6 = TP-6 for clarity. (**F**) Injection schema for comparing one-time (400,000 total, n = 10) cell dose and fractionated (2,400,000 total, n = 10) cell injections (left) and representative BLI images at endpoint (right). (**G**) Bar

graph depicting total flux emission in each group at experimental endpoint. (**H**) Schematic of scRNA-seq experiment conducted using a reversed BC.ID injection order. LARRY barcodes are readily captured by Chromium 10x Feature Barcoding. (**I**) Pie charts of RNA-level barcode frequencies in each location grouped as early (BC.ID5, BC.ID6), mid (BC.ID4, BC.ID3), and late (BC.ID2, BC.ID1). (**J**) Heatmap of sample level barcode frequencies, BC.ID6 = TP-1, BC.ID5 = TP-2, BC.ID4 = TP-3, BC.ID3 = TP-4, BC.ID2 = TP-5, BC.ID1 = TP-6. (**K**) Schematic (top) and MetTag BC.ID distribution (bottom) for independent TNBC lung metastasis model depicting enrichment of scRNA-seq derived early TP DTCs in the metastatic lung at endpoint. Data in Figure 1G was analyzed using a two-tailed Student's t test and graphed as mean with standard deviation (SD).

Figure 2: Clonal Analysis Reveals Shared Evolutionary Path Towards Inflammatory Signature

(**A**) Split UMAP depicting cluster distributions across the four experimental conditions and identifying cancer cell-enriched clusters in ascites and omentum. (**B**) Reclustered cancer cell UMAP colored by the two metastasis-bearing anatomical locations. (**C**) Stacked bar chart depicting the frequency of Seurat subclusters within each metastatic location. (**D**) Seurat cluster UMAP of reclustered cancer cells with transcriptional program labels. (**E**) Dot plot depicting Hallmark pathways across all subclusters used to define each cluster subset gene program in (D). (**F**) Schematic representation of the possible outcomes of LARRY clonal analysis based on transcriptome patterns of enriched clones. (**G**) Heatmap of normalized clonal LARRY barcode counts across the two anatomical locations and individual mice (HTOs). (**H**) UMAP overlay of top 3 expanded clones in the omentum. (**I**) Bar chart depicting the relative subcluster proportions present in each of the top 3 barcode clones. (**J**) scVelo-generated PAGA velocity graph indicating trajectory arrows and inferred cluster lineage. (**K**) scVelo and CellRank-based simulated path from start to endpoint clusters. (**L**) Violin plot depicting RNA-level contribution of each timepoint to the IFNγ signature. Data in Figure 2L was analyzed by first defining the IFNγ signature using canonical mouse genes, followed by

706 directly applying the wilcox.test() function in Seurat to compare TP-1 and TP-6
707 expression.
708

709 **Figure 3: Activation of IFNγ Response in Ascites is Necessary for Successful**
710 **Omental Colonization**

711 (**A**) DEG-based volcano plot of gene expression differences between OmMet and
712 AscMet, where threshold for significance was defined at $p < 0.05$ and $log2FC < -1.0$ for
713 downregulation or >1.0 for upregulation. (**B**) Boxplots comparing IFN signature modules
714 between AscMet and OmMet. (**C**) Schematic describing in vivo ovarian metastatic niche
715 signature screen. Partially created with BioRender.com. (**D**) In vivo CRISPR screen
716 RankView plots for all 100 genes generated using MAGeCKFlute. OmMet (n=5) and
717 AscMet (n=4) samples were compared to the original pool of ID8 cells. (**E**) Ranks of
718 individual sgRNAs targeting positive control Pten and depleted genes. (**F**) Lollipop plot
719 of depleted pathways associated with depleted genes in Fig. 3E. (**G**) IFNγ treatment
720 time course qPCR plots of select CRISPR hits and positive controls. (**H**) IFNγ treatment
721 time course western blot probing for Stat1/pStat1 and GBP1. (**I**) Schematic of in vivo
722 experimental metastasis study comparing sgNTC and sgIFNGR1.g1 groups. (**J**) Time
723 course log10-transformed total emission/flux values (left). Two independent groups
724 pooled; cohort 1 NTC; n = 8, KO; n = 7; cohort 2 NTC; n = 5, KO; n = 5. log10-
725 transformed flux plot for week six with p value (right). (**K**) Kaplan Meier survival curve
726 generated for cohort 1. (**L**) Experimental schematic for staggered sgIfngr1 (n = 4) or
727 sgNTC1 (n = 3) followed by sgNTC2-cell injection. (**M**) Representative endpoint BLI
728 images of metastasis bearing mice in each group (left) and endpoint BLI quantification
729 comparing tumor burden between sgIfngr1 and sgNTC first injection (right). (**N**)
730 Heatmap showing enrichment of first DTC seed - either sgNTC1 or sgIfngr1 - and 2nd
731 DTC seed, sgNTC2. DEG data in Figure 3A was analyzed using the FindMarkers()
732 function. Data in Figure 3B was analyzed by first defining custom IFN signatures,
733 followed by applying wilcox.test() in Seurat to compare module scores between AscMet
734 and OmMet. CRISPR screen related data (3D-3F) was analyzed using MAGeCK and
735 MAGeCKFlute. Data in 3G, 3J, 3K, and 3M was analyzed and graphed in Prism. 3G,
736 SJ, and 3M were analyzed using a standard t test; 3G and 3M data was plotted as

mean with SD, while 3J was plotted as median. Survival data in 3K was computed using a standard log-rank test.

Figure 4: IFNγ Pathway Mediates Resistance to Anoikis and Activates TNF Signaling and Dormancy Programs

(**A**) Cell-Titer Glo (CTG) assay luminescence values graphed as fold change for regular culture conditions (left) and ultra-low attachment (ULA) conditions (right), with and without IFNγ treatment. (**B**) Volcano plots generated from bulk RNA-seq depicting top DEGs between sgNTC (wild type) cells under regular culture conditions with or without IFNγ treatment (left) and under ULA conditions with and without IFNγ treatment (right). (**C**) Venn diagram showing 25 overlapping and 30 unique upregulated genes in sgNTC cells treated with IFNγ under ULA conditions. (**D**) Heatmap of vst-normalized gene counts for ULA-specific upregulated genes. (**E**) Bar plot depicting top 15 Reactome pathways upregulated under ULA conditions in cells treated with IFNγ. (**F-G**) CTG flux dot plots for Stat1-KO (F) and Irf1-KO (G) cells under ultra-low attachment, with or without IFNγ treatment. (**H**) Violin plots comparing expression level of immunoproteasome (Psmb10, Psmb9), DNA repair/apoptosis (Parp12, Parp14, Parp9), and immune checkpoint (Cd274) levels between OmMet and AscMet. (**I**) scRNA-seq based gating strategy used to identify $Irf1^{high}$ and $Irf1^{low}$ cells for module scoring. (**J**) Violin plots comparing expression level of Cd274 (left), Psmb10 (middle), and Parp14 (right) between $Irf1^{high}$ and $Irf1^{low}$ cells. Fold change in F4A was determined by normalizing each cell line's CTG value to the regular attachment, without IFNγ treatment. CTG assay luminescence data (4A) was graphed as mean and SD, data in 4F and 4G was graphed as median values. scRNA-seq based transcript expression levels were compared between $Irf1^{high}$ and $Irf1^{low}$ cells and OmMet/AscMet cells by applying the wilcox.test() function in Seurat. RNA-seq data was analyzed using DESeq2 and visualized as variance-stabilized counts.

Figure 5: Niche-specific Transcriptional States of Omental and Ascites-Derived TAMs

767 (**A**) Violin plots depicting CRISPR screen hits expression level across Broad cell ID
768 categories (cell types). (**B**) CellChat-generated circus plots of interaction strengths
769 between Broad cell ID categories in metastatic omenta (left) and ascites (right). (**C**)
770 Stacked bar chart of cell type proportions across the four experimental groups. (**D**)
771 UMAPs of reclustered myeloid cells, split by experimental condition. (**E**) UMAP of
772 subclustered myeloid cells overlayed with scVelo RNA velocity arrows. Arrows are
773 pointing from ascites TAMs (clusters 1 and 5) to omentum TAMs (clusters 0 and 6). (**F**)
774 DEG volcano plot comparing gene expression differences between ascites TAM cluster
775 1 and omentum TAM cluster 0. (**G**) Stacked bar chart of subsetted T/NK cells comparing
776 cell proportions in ascites and omentum. (**H-I**) Dot plots depicting Reactome pathways
777 enriched in ascites (H) and omentum-derived TAMs (I). Significance of DEGs in Figure
778 5F was evaluated by applying the FindMarkers() and Wilcoxon test in Seurat to
779 compare ascites and omental *Cd68*^{high}/*Adgre1*^{high} macrophages.
780
781 **Figure 6: Peritoneal Macrophages are Direct DTC Pro-Survival Interactors**
782 (**A**) Liposomal chlodronate-based macrophage depletion strategy and timeline
783 schematic with representative tissue images. Omental tumor burden quantification and
784 flow-based ascites quantification (bottom). Control group; n= 7, and Chlodrosome; n =
785 7. (**B**) Schematic describing Cre-based NicheTracing labeling system where ID8 and
786 E0771 cancer cells express Cre.ERT2. Upon nuclear entry of Cre.ERT2 into Ai6
787 reporter niche cells, labeled niche cells turn ZsGreen positive. (**C**) Representative gating
788 strategy depicting the major cell population tagged with zsG. (**D**) Quantification of
789 F4/80+ and TREM2 mean fluorescent intensity (MFI) of contacted, ZsGreen high cells.
790 (**E**) Volcano plot comparing DEGs between metastasis-infiltrating Trem2-low and
791 Trem2-high macrophages. (**F**) Schematic depicting mouse model for macrophage-
792 specific Trem2 knockout. (**G**) Log transformed BLI-derived flux values in Trem2fl/fl (wild
793 type; n = 5) and Lys2-Cre/Trem2fl/fl (knockout; n = 5) mice at metastasis endpoint. Mice
794 were injected with ID8 p53-/- Luciferase cells. (**H**) Schematic of macrophage-cancer cell
795 coculture layout (top) and representative coculture images for one cell line (bottom). (**I**)
796 Plots of percent CD45 negative cancer cell viability (ZombieAqua negative) post
797 coculture in three cell lines. (**J**) Stacked bar chart of main cell type proportions captured

in human scRNA-seq dataset across five anatomical locations, using maintype-2 annotation provided by publisher. (**K**) Venn diagram of top NicheNet predicted ligands after filtering for robust expression and overlapping with top ligands in our murine dataset. (**L**) Heatmap comparing enrichment of a curated list of receptors in bulk RNA-seq comparing ULA-cultured cells treated with IFNγ and regular attachment conditions. Data in Figures 6D was plotted as mean with SD and differences between groups were compared via a two-tailed unpaired Student's t test. Data in Figures 6I was similarly analyzed using a Student's t test and plotted with median values. Data in Figure 6E was analyzed using the FindMarkers() function in Seurat and Wilcoxon test to compare gated Trem2-low and Trem2-high cells. RNA-seq heatmap data in 6L was analyzed using DESeq2 and visualized as variance-stabilized counts.

SUPPLEMENTAL INFORMATION (Including Supplemental Figures S1-S9)

Figure S1. MetTag Tracing Construct and Metastatic Model Validation

(A) Schematic depicting MetTag library barcoding plasmid, and modes of detection upon plasmid integration: DNA level, Pol III U6 driven RNA level, and Pol II CROP-seq based. (B-C) Barcode frequencies comparing relative evenness of library distribution across BC.ID batches (B) and original depositor LARRY library (C). (D) Table depicting unique reads detected in each library batch after MiSeq sequencing and read filtering. (E) Representative ascites images and dissecting scope images of GFP+ metastases formed under the repeated injection schema in wild type (n = 4) and NRG mice (n = 4). (F) Separate cohort of mice were subjected to ID8 p53-/- Luciferase injection and omental burden was quantified via ex vivo BLI imaging (top) and by measuring omental weights (bottom). (G) Representative ascites images and dissecting scope images of GFP+ metastases formed under the repeated injection schema in liposome (n = 4) and chlodrosome treated mice (n = 4). (H) Barchart depicting macrophage depletion efficiency (left) and quantification of GFP+ cells (right) in ascites under macrophage. Data in Figures S1H and S1F was analyzed in GraphPad Prism and plotted as mean

827 with SD and differences between groups were compared via a two-tailed unpaired
828 Student's t test.

829

830 **Figure S2. scRNA-seq-based Tumor Cell Identification and Cancer Cell Velocity**

831 (**A**) Feature plot of main marker genes used to define and subset cancer cells. (**B**)
832 Heatmap of reclustered cancer cell marker genes. (**C**) Violin plots of top defining cluster
833 marker genes. (**D**) Escape generated Hallmark pathways each represented by a
834 different color. (**E**) Escape pathway-based violin plots of each pathway class in (D). (**F**)
835 UMAPs depicting main pathway signatures represented in the top three clonally
836 expanded barcoded cells. (**G**) CellRank-generated initial and terminal cellular states
837 overlayed on the cancer cell UMAP (top) and violin plot of IFNα signature score across
838 the six different BC.ID timepoints (bottom). (**H**) UMAP of captured single cells in TNBC
839 lung metastasis model (left) and RNA-based gating strategy to subset non-immune cells
840 for subsequent barcode analysis. (**I**) Heatmap depicting enriched clonal LARRY
841 barcodes in each lung samples. IFNα signature data in Figure S2G was plotted by first
842 defining the IFNα signature using Hallmark IFNα response genes, followed by directly
843 applying the wilcox.test() function in Seurat to compare expression level differences
844 between TP-1 and TP-6 groups.

845

846

847 **Figure S3. IFN Signaling in Metastatic Niches & *In vivo* CRISPR Screening**

848 (A) UMAP of captured cancer cells colored by in vivo (Lung.Met) and in vitro
849 (E0771.cell) cell line. (B) Hallmark pathway analysis on DEG list comparing in vivo vs. in
850 vitro. Module scores comparing IFNγ (C) and IFNα (D) genes between in vivo and in
851 vitro. (E) VlnPlots of individual IFNγ response related genes. (F-G) Dot plots of Hallmark
852 pathways based on DEGs between AscMet and OmMet. (H) Heatmaps depicting IFN
853 response gene scoring differences between AscMet and OmMet. (I) Western blot
854 validation of SpCas9 expression in ID8 p53-/- cells after PiggyBac transposon
855 transfection and selection with hygromycin. (J) Representative flow cytometry generated

histogram of mCherry fluorescence (left) and bar chart depicting percent mCherry positive cells five days after lenti-guide transduction (right). (K) Violin plot of Ifngr1 expression levels in cancer cells in vivo. (L) Representative flow cytometry generated histogram of IFNGR1 surface expression in knockout vs. wild type cells (left) and bar chart with quantification of IFNGR1 mean fluorescent signal changes (right). (M) Western blot probing for IFNγ downstream transcriptional targets, Stat1 and Gbp2b, in Ifingr1 knockout cells. (N) Endpoint (week six) BLI images of sgIfngr1 (n = 7) compared to sgNTC experiment mice (n = 8). (O) KMPlotter-generated Kaplan Meier progression free survival curve comparing low and high IFNGR1 expression at stage III and stage IV. IFNγ/IFNα signatures in Fig. S3C and S3D were described in previous figures. Data in S3J and S3L was analyzed in GraphPad Prism using a two-tailed Student's t-test and graphed as mean with SD. Figure 3C-D module scores and S3K transcript level violin plot values were compared using the wilcox.test() function in Seurat.

Figure S4. IFNγ-induced Pro-Survival and Dormancy Programs

(A) Clonogenic assays in absence and presence of recombinant IFNγ, with or without IFNGR1 knockout. (B) Schematic depicting in vitro bulk RNA-seq experiment comparing ULA and regular culture conditions under IFNγ treatment. (C) PCA plot of sequenced RNA-seq groups. Each dot represents a different sample; color represents different treatment or culture condition. (D) MA plot showing differentially expressed genes (DEGs) between ULA and regular culture conditions. Blue points indicate significant genes (padj < 0.05, log2FC>+/- 1). (E) Bar plot depicting top Reactome pathways enriched in ULA compared to regular culture conditions. (F) S and G2/M cell cycle gene heatmap comparing sgNTC cells cultured under ULA and regular culture conditions. (G) Heatmap of top DEGs (both unique and overlapped with regular culture) between ULA and regular culture. (H) Western blots showing protein levels of Stat1, Irf1, and Gbp2b under Stat1 (left) or Irf1 (right) knockout, with IFNγ treatment. (I) Kaplan-Meier survival curves for ovarian cancer patients stratified by early stage (left) and late stage (right) and by high and low expression of PARP14. Data in (A) was plotted in GraphPad Prism and analyzed using a Student's t test. The PCA plot was generated from variance-

886 stabilized transformed (VST) counts. Progression free survival Kaplan-Meier curves
887 were generated using KMplotter.

888

889 **Figure S5. Related to Main Figure 5; Additional macrophage and T/NK cell**
890 **analysis**

891 (A) UMAP depicting all cells captured across four sequenced groups. (B)
892 "Broad_cell.ID" classification of Seurat clusters into cell types based on cluster marker
893 genes. (C) CellChat generated bar charts depicting number of interactions (left) and
894 interaction strength (right) across the four sample groups. (D) Heatmap of myeloid TAM
895 subclusters 1, 0, 5, and 6. (E) Violin plots showing gene expression of canonical TAM
896 markers across myeloid subclusters. (F) Volcano plot of DEGs between myeloid cluster
897 5 and 6. (G) Dot plot of GO Biological Process pathways upregulated in omentum-
898 derived T/NK cells based on the DEG list comparing to ascites-derived T/NK cells. (H)
899 RNA-based gating strategy to subset out macrophages for subsequent analysis. (I)
900 Biaxial scatter plot of M1 and M2 module scores with overlapped ascites and omental
901 TAMs. (J) Violin plots comparing individual genes belonging to cellular response to
902 stress (Anxa1, Hmox1) and cellular respiration (Ndufb8, Cox5a) pathways between
903 omental and ascites TAMs. (K) Flow cytometry analysis plots of cancer and immune cell
904 frequencies in naïve and metastatic settings: frequency of GFP+ cancer cells,
905 CD11b+/CD11c+ double positive myeloids, CD11b-/CD11c+ dendritic cells,
906 CD11b+/F4/80+ macrophages, and frequency of CD8+ T cells. In (F), DEG analysis
907 was performed using the FindMarkers() function in Seurat and significance determined
908 via Wilcoxon test. Fig. S4I hybrid score and S4J violin plot expression levels were
909 compared using the wilcox.test() function in Seurat. Flow cytometry data in S5K was
910 analyzed via two-tailed unpaired Student's t test and plotted with median values.

911

912 **Figure S6. Related to Main Figure 6; NicheTracing Validation & Trem2-knockout**

913 (**A**) Western blot validation of Cre expression in target cell lines: E0771 murine TNBC
914 line and ID8 ovarian cancer cell line. (**B**) Schematic depicting Cre reporter used to

915 transfect HEK293T cells and Cre constructs expressed by target cells for in vitro color
916 switch assays. (**C-F**) Images generated after 72 hours of coculture with or without 2 uM
917 4-OHT treatment. (**G**) Representative dissecting microscope images of negative control
918 spleen and lugs collected 2 weeks post E0771 retro-orbital injection. (**H**) Flow cytometry
919 bar plots at experimental endpoint showing percent switched immune cells (ZsG+) with
920 or without tamoxifen treatment (left) and within the tamoxifen treated group, frequency
921 of ZsG+ macrophages compared to ZsG- (right) in metastatic lungs. (**I**) Bar plot showing
922 frequency of ZsG+ CD11b myeloids compared to ZsG- in ascites. (**J**) Representative
923 flow cytometry gating for TREM2 macrophage enrichment in ZsG+ fraction. (**K**) scRNA-
924 seq gating strategy to subset TREM2-high and low TAMs. (**L**) Go Biological Processes
925 pathways upregulated in Trem2-high (left) and Trem2-low (right) TAMs. (**M**)
926 Macrophage-specific Trem2 depletion validation. Flow cytometry data in (S6H-I) was
927 analyzed using a two-tailed unpaired Student's t test and plotted as mean with SD.

928

929 **Figure S7. Related to Main Figures 5 & 6; Immunotyping and Flow Cytometry**
930 **Gating Strategies**
931 (**A**) Flow gating strategy for macrophage depletion study (left) and representative gates
932 for F4/80 macrophages in FMO, liposome control, and chlodrosome treated groups
933 (right). (B-**C**) Flow gating strategy for assessing MHC-II+/CD11b+ macrophage
934 enrichment following F4/80 magnetic bead isolation from peritoneal cavity. Bar plot
935 showing relative enrichment of macrophage populations before the start of coculture.
936 (**D**) Flow gating strategy to assess CD45- cancer cell viability (Zombie Aqua negative
937 populations) after co-culture completion. Flow cytometry data in (S7A) was analyzed via
938 two-tailed unpaired Student's t test and plotted with median values.
939

940 **Figure S8. Related to Main Figure 6; Patient & Murine NicheNet Analysis**
941 (A) UMAP depicting all (>200,000) single cells collected from five locations and
942 annotated by cell type ("Maintypes-2"). (B) Heatmap of DEGs between Ascites and
943 Met.Ome-derived macrophages. (C) Dot plots depicting top GO molecular function
944 pathways expressed in patient omental TAMs (left) and ascites TAMs (right). (D)
945 NicheNet heatmap depicting top receptor-ligands pairs in murine ascites. (E) NicheNet

946 heatmap depicting top receptor-ligands pairs in patient ascites. (F) Bubble plot depicting
947 NicheNet-derived ligand expression among Maintypes-2 clusters. (G) Dot plot of GO
948 pathways enriched in cancer cells based on regulatory potential and downstream genes
949 affected by macrophage ligands. DEG analysis in Figure S8B was performed using the
950 FindMarkers() function in Seurat.
951
952
953 **METHODS**
954 ***Experimental Models***
955 **Mice**
956 All animal experiments were conducted according to IACUC protocols which were pre-
957 approved by the University of Notre Dame and UT Southwestern Medical Center IACUC
958 committees. Mice were housed with unlimited access to food and water in a
959 temperature-controlled holding room with a standard 12-hour light/dark cycle. Health
960 checks were performed daily during *in vivo* experiments. Wild type C57BL/6J (B6) mice
961 were 8-10 weeks old at the experiment onset. Control and treated transgenic mice were
962 age-matched, greater than 8 weeks of age. All experiments were carried out exclusively
963 on female mice.
964 C57BL/6J (B6, 000664), NOD.Cg-*Rag1*^{tm1Mom}*Il2rg*^{tm1Wjl}/SzJ (NRG, 007799), B6.Cg-
965 *Gt(ROSA)*$^{26Sortm6(CAG\text{-}ZsGreen1)Hze}$/J (Ai6, 007906), and B6J.129(Cg)-
966 *Gt(ROSA)26Sor*$^{tm1.1(CAG\text{-}cas9*,\text{-}EGFP)Fezh}$/J (Cas9 026179) mice were obtained from
967 Jackson Laboratory (Ben Harbor, ME). We generated Lyz2-Cre(+/-)/Trem2(fl/fl) double
968 transgenic mice by breeding Lyz2-Cre heterozygous (+/-) mice with Trem2(fl/fl). These
969 lines were generous gifts from the Zhong Lab at UT Southwestern Medical Center.
970
971 **Cell Lines**
972 The TNBC E0771 cell line (CH3 Biosystems, Amherst, NY; Cat.No. 940001-Vial) was
973 maintained in RPMI-1640 media supplemented with 10%FBS and 1%
974 Penicillin/Streptomycin (Pen/Strep). ID8 p53$^{-/-}$, ID8 p53$^{-/-}$ BRCA2$^{-/-}$, and PPNM ovarian
975 cancer cell lines, provided by the Stack lab at the University of Notre Dame, were
976 maintained in DMEM low glucose media with 5% FBS, 1% Pen/Strep, and 1% Insulin-

977 Transferrin-Selenium (ITS). PPNM cell media was additionally supplemented with 100
978 ng/ml Cholera toxin and 2ng/mL epidermal growth factor (EGF). HEK293T cells were
979 cultured in DMEM high glucose supplemented with 10% FBS, 1% Pen/Strep, and 1%
980 GlutaMAX (Gibco, 35050061). Cell cultures were grown at 37 ºC, 5% CO_2, and 95%
981 humidity. All cell lines were tested and were negative for mycoplasma contamination
982 using a routine mycoplasma PCR kit (ABM).
983
984 **Establishment and Monitoring of Experimental Metastasis**
985 For the single-injection OvCa model, $4x10^5$ ID8-LARRY.GFP or ID8-Luciferase were
986 injected into the peritoneal cavity. To ensure adequate library coverage, $2.4x10^6$ ID8-
987 Cas9.Lib tagged cells were injected for CRISPR screening experiments (>1000x
988 coverage). In the repeated injection model, mice received $4x10^5$ cells per injection,
989 administered six times over the course of 12 days. Mice were typically sacrificed 6
990 weeks after initial dose of cancer cells. $6x10^5$ E0771-LARRY.GFP or E0771-Luciferase
991 tagged cells were injected into the retro-orbital sinus of mice for one time injection lung
992 metastasis model or $1.5x10^5$ cells in six separate injections for the repeated injection
993 model. Mice were sacrificed between 14-18 days in both experimental models. For
994 monitoring metastasis in luciferase-expressing models, 100 ul of D-luciferin (15 mg/mL
995 stock, GoldBio cat#: LUCK-500) was administered intraperitoneally and imaged using
996 an AMI-HTX spectral imaging instrument. The total emission (flux) data for each region
997 of interest (ROI) was obtained after image analysis using the Aura software.
998
999 **Macrophage Depletion**
1000 Macrophage depletion was achieved using encapsulated liposomal chlodronate
1001 (Encapsula Nano Sciences, SKU# CLD-8901). Mice received a pre-treatmeant with 200
1002 ul chlodrosome or empty liposome nanoparticles i.p. 24 hours before cancer cell
1003 injection. Following pre-treatment, 100 ul of chlodrosome was administered twice
1004 weekly throughout the study duration.
1005
1006 **Individual Gene Knockout Guide Cloning**

The CROP-seq-V2 plasmid (Addgene # 127458) was first modified to include a P2A-mCherry sequence downstream of the puromycin resistance gene (PuroR) through a NEBuilder HiFi DNA Assembly (NEB, E5520S) reaction. Then, single-guide RNA (sgRNA) sequences were designed using CRISPick (Mouse GRCm38 reference genome), oligos synthesized by IDT with BsmBI overhangs, annealed, and cloned into the modified CROP-seq-V2 plasmid using the NEBridge Golden Gate Assembly Kit (NEB, E1602S). The resulting plasmids were first transformed into competent *E. coli*, plated on LB-ampicilin (AMP) plates, and grown at 30 ºC, before plasmid extraction. Below are the sgRNA sequences used for gene targeting, including the necessary BsmBI overhangs:

sgNTC-1 Top oligo

5'- **CAC CG**A CCT GAT ACG TCG TCG CGT A -3'

sgNTC-1 Bottom oligo

5'- **AAA C**TA CGC GAC GAC GTA TCA GGT **C** -3'

sgNTC-2 Top oligo

5'- **CAC CG**G TAT TAC TGA TAT TGG TGG G -3'

sgNTC-2 Bottom oligo

5'- **AAA C**CC CAC CAA TAT CAG TAA TAC **C** -3'

sgIrf1 guide 1 Top oligo

5'- **CAC CG**T GGA AGC ACG CTG CTA AGC A -3'

sgIrf1 guide 1 Bottom oligo

5'- **AAA C**TG CTT AGC AGC GTG CTT CCA **C** -3'

sgIrf1 guide 2 Top oligo

5'- **CAC CG**C TGT AGG TTA TAC AGA TCA G -3'

sgIrf1 guide 2 Bottom oligo

5'- **AAA C**CT GAT CTG TAT AAC CTA CAG **C** -3'

sgStat1 guide 1 Top oligo

5'- **CAC CG**T ATC CTG TGG TAC AAC ATG C -3'

sgStat1 guide 1 Bottom oligo

5'- **AAA C**GC ATG TTG TAC CAC AGG ATA **C** -3'

sgStat1 guide 2 Top oligo

5’- **CAC CG**G CAA GCG TAA TCT CCA GGT A -3’

sgStat1 guide 2 Bottom oligo

5’- **AAA C**TA CCT GGA GAT TAC GCT TGC **C** -3’

sgIfngr1 guide 1 Top oligo

5’- **CAC CG**G GCT CGG AGA GAT TAC CCG A -3’

sgIfngr1 guide 1 Bottom oligo

5’- **AAA C**TC GGG TAA TCT CTC CGA GCC **C** -3’

sgIfngr1 guide 2 Top oligo

5’- **CAC CG**T ATA CCA ATA CGC AAA TAC C -3’

sgIfngr1 guide 2 Bottom oligo

5’- **AAA C**GG TAT TTG CGT ATT GGT ATA **C** -3’

Library Cloning

Six MetTag-LARRY-BC.ID libraries were generated via overhang PCR by amplifying the region within the original pLARRY-eGFP plasmid containing random barcodes. Primers were designed with overhangs containing: (1) a unique 6-nucleotide library identifier (ID), (2) a chromium 10x capture sequence, and (3) BsmBI restriction sites flanking both ends of the barcode (synthesized by Sigma-Aldrich). Amplified barcode fragments were introduced into the pRG212 third-generation lentiviral plasmid using the NEB Golden Gate Assembly Kit (NEB, E1602S) at a 2:1 insert-to-vector molar ratio. The cloning reaction was transformed into Endura electrocompetent *E. coli* cells (Biosearch Technologies, 60242-1) and plated overnight on LB-AMP plates. $3x10^6$-$2x10^7$ CFU colonies were harvested by flushing prewarmed LB broth and cultured for 2 hours in liquid LB. sgRNA oligo pools were synthesized as oPools (IDT), containing BsmBI cloning compatible overhangs. The oligos were then annealed and introduced into the CROP-seq-V2.mCherry lentiviral plasmid using the NEB Golden Gate Assembly Kit as described above. Approximately 5x10^7 CFUs for OvCa library and 2x10^7 colonies for MetTag library were harvested for maxiprep. For both LARRY barcode and CRISPR libraries, plasmids were purified using the ZymoPURE II Plasmid Maxiprep kit (Zymo Research, D4202). The MetTag-LARRY-BC.ID vector map and CROP-seq-V2.mCherry vector map will be made available on Addgene upon publication.

1069

1070 **Plasmid Library Amplification and Diversity Validation**

1071 Plasmid DNA was amplified using two step PCR to first amplify and then add indexing
1072 sequences to libraries. First round PCR was conducted using custom P5 and P7
1073 adapters with overhangs compatible with Nextera indexing primers, followed by cleanup
1074 with Agencourt AMPure XP beads (Beckman Coulter, NC9933872) at a 1.8x bead ratio
1075 to remove primers. Index PCR reaction was conducted as outlined in the Illumina 16S
1076 Metagenomic Sequencing Library Preparation manual (Illumina, Doc #15044223, page
1077 11-12) using 2x KAPA HiFi HotStart ReadyMix (Roche, KK2601) and Nextera XT Index
1078 kit v2 primers (Illumina, FC-131-1001). Final indexed libraries were quantified via the
1079 Qubit HS assay kit. LARRY libraries were run on a Bioanalyzer instrument and
1080 sequenced on an Illumina MiSeq instrument. CRISPR libraries were run on TapeStation
1081 using the High Sensitivity D1000 assay (Agilent, 5067-5585, 5067-5594) and
1082 sequenced on a NovaSeq-X instrument. Demultiplexed fastq files were filtered for high
1083 quality reads, and the number of unique reads was quantified. For the CRISPR libraries,
1084 a customized script was used to estimate the percentage coverage based on the
1085 original guide RNA whitelist.

1086

1087 **Lentivirus Production and Target Cell Transduction**

1088 MetTag-LARRY-BC.ID, CROP-seq-V2.mCherry guide, or Lenti-Luciferase.P2A.Neo
1089 (Addgene # 105621), and second-generation lentiviral packaging plasmids were
1090 transfected into HEK293T cells along with the CalFectin transfection reagent
1091 (SignaGen, SL100478). Lentivirus was harvested after 72 hours and concentrated
1092 (Lenti-X Concentrator, Takara Bio, 631231). Concentrated lentivirus was added to target
1093 cells along with 8 ug/ml polybrene. To achieve low MOI for CRISPR screening
1094 experiments, ID8 p53$^{-/-}$ ovarian cancer cells were infected at a low multiplicity of
1095 infection (MOI) of 0.15, as calculated by the percentage of mCherry-positive cells 48
1096 hours post transduction. 48 hours post transfection, cells were selected with either
1097 G418 (pRG212-LARRY; Sigma-Aldrich, 4727878001) or puromycin (CROP-seq-
1098 V2.mCherry; Invivogen, ant-pr-1) for a minimum of 7 days.

1099

1100 **Genomic DNA (gDNA) Amplicon Library Preparation**
1101 Genomic DNA was extracted from cultured cells and digested tissues using either the
1102 Quick-DNA Midiprep Kit (Zymo Research, D4075) or the Quick-DNA Miniprep Plus Kit
1103 (Zymo Research, D4068), depending on the starting cell number. Extracted DNA yield
1104 was quantified via a NanoDrop spectrophotometer, and samples were normalized to the
1105 same, lowest input concentration prior to PCR. Two rounds of PCR amplification were
1106 performed on > 200 ng starting gDNA material. The first round was utilized for amplicon
1107 amplification with nested primers for 15-20 cycles using a high-fidelity hot start
1108 polymerase, followed by purification with a 1.8x bead-to-sample AMPure XP bead ratio.
1109 Eluted amplicon DNA was quantified using the Qubit high sensitivity (HS) assay kit
1110 (Thermo Fisher Scientific, Q33231) and concentrations normalized prior to indexing.
1111 Approximately 5 ng of DNA was carried into the index PCR rection, which was
1112 conducted similarly to the plasmid library construction protocol described above. Index
1113 products were purified using the same AMPure XP beads ratio to remove excess
1114 primers. Library quantity was assessed via the Qubit HS assay kit and analyzed on a
1115 TapeStation instrument using the High Sensitivity D1000 assay to confirm expected
1116 library size and distribution. LARRY gDNA libraries were sequenced in-house on an
1117 Illumina MiniSeq instrument (Mid output kit, 300 cycles) while CRISPR gDNA libraries
1118 (101 genes*10 guides per gene, 20 non targeting guides = 1,030 guides) were
1119 sequenced on a NovaSeq-X instrument. High quality reads were filtered and analyzed
1120 via two parallel approaches: LARRY barcode counts were extracted to quantify library
1121 batch identity (ID), while CRISPR libraries were processed using the MAGeCK pipeline
1122 to identify enriched or depleted guide RNAs. Primers used for amplification were as
1123 follows:
1124 LARRY Round 1 PCR REV, Tm: 55.9:
1125 5’ – GTC TCG TGG GCT CGG AGA TGT GTA TAA GAG ACA GTG GGG AAT TTC TAC
1126 TCT TGT AGA TCG – 3’
1127 LARRY Round 1 PCR FWD Stagger, Tm: 59.0:
1128 5’-TCG TCG GCA GCG TCA GAT GTG TAT AAG AGA CAG CTT GCT AGG ACC GGC
1129 CTT AAA GC -3’
1130 CRISPR Round 1 PCR REV, Tm: 51.0:

5’ – GTC TCG TGG GCT CGG AGA TGT GTA TAA GAG ACA GTT CTT GGC TTT ATA TAT CTT GTG G– 3’

CRISPR Round 1 PCR FWD Stagger, Tm: 53.0:

5’ – TCG TCG GCA GCG TCA GAT GTG TAT AAG AGA CAG CTC AAG TTG ATA ACG GAC TAG C– 3’

PiggyBac Transposon Transfection

SpCas9 and CreERT2 coding sequences were cloned into PiggyBac transposon plasmids containing a hygromycin resistance cassette via Gateway cloning (ThermoFisher Scientific, 11791020 & 11789020). Target cells were plated in 6-well plates 24 hours prior to transfection. Five ug of the SpCas9 or 1 ug of CreERT2 PiggyBac plasmid was co-transfected with 0.5 ug of Super PiggyBac Transposase (System Biosciences, PB210PA-1), along with the Calfectin transfection reagent. The transfection mixture was added to cells in a dropwise manner. 12-16 hours post transfection complete growth media was replenished. Forty-eight hours post transfection, cells were selected with hygromycin B (Corning, 30-240-CR) for a minimum of 10 days to enrich for successful transgene integrated cells.

Cell Preparation for Single-Cell RNA Sequencing

Naïve and tumor bearing mice were sacrificed via cervical dislocation six weeks following initial cancer cell injection. To collect peritoneal cells, 5 mL of cold 1xHBSS was injected intraperitoneally using a 25G needle, followed by lavage and peritoneal fluid retrieval using a 20G needle. Omenta were excised from the peritoneal cavity and examined under a dissecting microscope to confirm the presence of macroscopic metastases. Omental tissues were then minced and digested for 30 minutes at 37ºC in RPMI-1640 medium containing 0.4% collagenase type II (Gibco, 17101015), 50 ug/ml DNAseI, and 0.1% BSA. Following digestion, cell suspensions were passed through a 70-uM strainer and washed with cold 1xPBS. Lavage, ascites, and omental samples were resuspended in 1x RBC lysis buffer (BioLegend, 420301) to remove red blood cells. To prepare for single-cell analysis, omental samples were stained with ZombieRed (BioLegend, 423109) to exclude dead cells and sorted via FACS. Sorted cells were then

1162 prepared for 10X Genomics Chromium Single Cell Gene Expression analysis. For
1163 TNBC lung sample scRNA-seq, mice were perfused with 5mL of ice cold 1xPBS, lungs
1164 were collected and imaged using the GFP channel on a dissecting scope. Lungs with
1165 detectable tumor burden were cut into small pieces and processed into single cell
1166 suspensions by digestion with 1x collagenase/hyaluronidase (STEMCELL Technologies,
1167 #07912) and 0.15 mg/ml DNase I in serum free RPMI 1640 medium. After passing the
1168 digested samples through a 70-uM strainer and washing with serum free RPMI, the
1169 samples were lysed for RBCs and processed similarly to OvCa samples downstream. A
1170 detailed protocol for sample multiplexing via hashtags can be found in the CITE-seq/cell
1171 hashing protocol on the CITE-seq website (https://cite-seq.com/wp-
1172 content/uploads/2019/02/cite-seq_and_hashing_protocol_190213.pdf). In brief, samples
1173 were first blocked with FcR Blocking Reagent (Miltenyi Biotec, 130-092-575) in 50 uL of
1174 cell staining buffer for 20 minutes on ice. Samples were then stained with TotalSeq™-A
1175 hashing antibodies obtained from BioLegend, including:
1176 M-HTO-1 (M1/42; 30-F11, 155801),
1177 M-HTO-2 (M1/42; 30-F11, 155803),
1178 M-HTO-3 (M1/42; 30-F11, 155805),
1179 M-HTO-4 (M1/42; 30-F11, 155807),
1180 M-HTO-5 (M1/42; 30-F11, 155809),
1181 M-HTO-6 (M1/42; 30-F11, 155811),
1182 M-HTO-7 (M1/42; 30-F11, 155813),
1183 M-HTO-8 (M1/42; 30-F11, 155815).
1184 Staining was performed for 25 minutes on ice, followed by three washes with staining
1185 buffer (decreasing EDTA concentration per wash) and loading onto a 10X Genomics
1186 Chromium Controller.
1187
1188 **scRNA-seq Library Preparation and Illumina Sequencing**
1189 Single-cell transcriptomic libraries were prepared as outlined in the Chromium Next
1190 GEM Single Cell 3' Reagents Kits v3.1 with Feature Barcoding technology kit manual.
1191 Kits necessary for transcriptome library preparation were: Chromium Next GEM Single
1192 Cell 3' GEM, Library & Gel Bead Kit v3.1, 4 rxns (10x Genomics, PN-1000128),

Chromium Single Cell 3' Feature Barcode Library Kit, 16 rxns (10x Genomics, PN-1000079), Chromium Next GEM Chip G Single Cell Kit, 16 rxns (10x Genomics, PN-1000127), and Single Index Kit T Set A, 96 rxns (10x Genomics, PN-1000213). Hashtag libraries were prepared using the standard CITE-seq protocol (https://cite-seq.com/wp-content/uploads/2019/02/cite-seq_and_hashing_protocol_190213.pdf). LARRY-BC.ID barcode libraries were constructed using a custom nested PCR protocol followed by indexing. Primers required for LARRY-BC.ID library preparation included:

Round 1 PCR FWD, Tm: 61.0

5' – *GCA GCG TCA GAT GTG TAT AAG AGA CAG* – 3'

Round 1 PCR REV: 45.0

5' – <u>CCT TGG CAC CCG AGA ATT CCA aat ttc tac tct tgt aga t</u> – 3'

Index PCR FWD, Tm: 61.0

5' – AAT GAT ACG GCG ACC ACC GAG ATC TAC ACT CGT CG*G CAG CGT CAG ATG TGT ATA AGA GAC AG* – 3'

Index PCR REV (ADT-RPI-1), Tm 61.0:

5' – CAA GCA GAA GAC GGC ATA CGA GAT CGT GAT GTG ACT GGA GTT <u>CCT TGG CAC CCG AGA ATT CCA</u> – 3'

{Partial Read 1N; LARRY transcript (lowercase), <u>P7 adaptor</u>*,* RPI1 **index***}*

The quality and quantity of the three individual libraries (transcriptome, HTO, and LARRY) were assessed via Qubit and TapeStation prior to sequencing. Libraries were pooled for sequencing on an Illumina NovaSeq X Plus platform with paired end reads (PE150).

scRNA-seq Data Analysis

Raw fastq files generated from the sequencing runs (mRNA, HTO, LARRY outputs) were processed through the 10x Genomics CellRanger pipeline v.7.2 to generate count matrices. Gene expression (mRNA) reads were aligned to a custom mouse reference genome containing fluorescent marker transcripts (mm10_3.0.0_FPs). Data from two different chromium 10x lanes, ascites lane and omentum lane, were merged using the

1224 SCT-normalized dataset integration method. Details related to integration steps can be
1225 found at: https://satijalab.org/seurat/articles/. In brief, individual lane single cell data was
1226 normalized for HTO (HTOdemux) followed by SCTransform prior to integration.
1227 Downstream analyses including dimensional reduction via principal component analysis
1228 (PCA), clustering and UMAP embedding, and differential gene expression (DEG)
1229 analysis were performed in RStudio under the Seurat package (v4.0)[18]. Cell type
1230 identities were assigned based on cluster marker genes. Subcluster level labels
1231 indicating different cellular statuses were determined through a combination of cluster
1232 marker genes and examining enriched pathways. RNA velocity analysis was performed
1233 in Python using scVelo and CellRank. Loom files were generated for each lane and
1234 merged, followed by Seurat object conversion to H5AD format. Metadata containing
1235 clustering and HTO information was integrated into the SCANPY anndata object. More
1236 details on the CellRank method can be found at:
1237 https://cellrank.readthedocs.io/en/latest/index.html. NicheNetR and CellChat were
1238 performed in RStudio. Sender and receiver cell types were selected prior to NicheNetR
1239 analysis. scRNA-seq expression data was analyzed using the Wilcoxon rank sum test
1240 either through the direct function wilcox.test() when assigning custom module scores or
1241 through the FindMarkers() function as part of the standard DEG analysis. Adjusted p
1242 values <0.05 were considered significant. Over-representation analysis (ORA) was
1243 performed on a filtered list of upregulated or downregulated genes from DEG analysis
1244 and the ReactomePA and clusterProfiler RStudio packages. org.Mm.eg.db package was
1245 used to convert genes to Entrez ID symbols. Adjusted p values <0.05 and log fold
1246 change > (+/-) 0.25 were considered significant. ORA uses Fisher's exact test to
1247 determine enriched gene sets. For Single Cell Gene Set Enrichment Analysis
1248 (ssGSEA), we utilized the Escape R package.
1249
1250 **Flow cytometry**
1251 Samples were extracted and pre-processed similarly as the scRNA-seq samples.
1252 Following tissue digestion of lung or omentum tissues and RBC lysis, digested samples
1253 were washed in 1x Flow Staining Buffer (Tonbo Biosciences, TNB-4222-L500). For
1254 viability assessment, cells were incubated with ZombieAqua Fixable Viability Kit

1255 (BioLegend, 423102) at a 1:750 dilution in 1xPBS for 20 minutes at room temperature.
1256 Following viability staining, cells were blocked with 1x FcR Blocking Reagent (Miltenyi
1257 Biotec, 130-092-575) to minimize nonspecific antibody staining. Cells were then stained
1258 with a combination of the following fluorochrome-conjugated surface antibodies: Pacific
1259 Blue™ anti-mouse CD45 (BioLegend, 157211, S18009F), APC/Fire™ 750 anti-mouse
1260 CD3 (BioLegend, 100247, 17A2) or PE/Cyanine7 anti-mouse CD3 (BioLegend, 100219,
1261 17A2), PE anti-TREM-2 (BioLegend, 824805, 6E9), APC anti-mouse CCR5 (BioLegend,
1262 107011, HM-CCR5), Brilliant Violet 605™ anti-mouse/human CD11b (BioLegend,
1263 101237, M1/70), APC anti-mouse I-A-I-E (BioLegend, 107613, M5/114.15.2), Brilliant
1264 Violet 711™ anti-mouse CD4 (BioLegend, 100447, GK1.5), PE/Dazzle™ 594 anti-
1265 mouse NK-1.1 (BioLegend, 156517, S17016D) or PE anti-mouse NK-1.1 (BioLegend,
1266 156503, S17016D), Brilliant Violet 421™ anti-mouse PD-L1 (BioLegend, 124315,
1267 10F.9G2), PE/Cyanine7 anti-mouse CD8a (BioLegend, 100721, 53-6.7) or
1268 APC/Cyanine7 anti-mouse CD8a (BioLegend, 100713, 53-6.7), Brilliant Violet 785™
1269 anti-mouse F4/80 (BioLegend, 123141, BM8). Cancer cells harvested from culture were
1270 similarly stained with ZombieAqua, FcR blocked, and then incubated with IFNGR1
1271 Recombinant Rabbit Monoclonal Antibody FITC (Invitrogen, MA5-46853, 062) with the
1272 corresponding Rabbit IgG Isotype Control FITC, eBioscience™ (Invitrogen, 11-4614-
1273 80). Cells were then washed with staining buffer, followed by analysis on a Cytek
1274 Northern Lights flow cytometer. FCS files were exported and analyzed using FlowJo
1275 (BD Biosciences).
1276
1277 **Western Blotting**
1278 Cells were plated at a density of 250,000-500,000 cells per 10 cm dish for regular
1279 attachment plate experiments. For anoikis assays, 3x 6 wells per sample were seeded
1280 with 300,000 cells each. The next day, cells were either treated with vehicle (1xPBS) or
1281 100 ng/ml mouse recombinant IFNγ (PeproTech, AF-315-05-100UG). After treatment,
1282 cells were harvested, washed with 1xPBS, and lysed in M2 lysis buffer (50 nM Tris-HCl,
1283 pH 7.4, 150 mM NaCl, 1% Triton X-100, 0.5 mM EDTA) with 1x Protease/Phosphatase
1284 Inhibitor Cocktail (CST, 5872). Cells were lysed for 1 hour on ice before centrifugation at
1285 high speed to collect protein lysates. Protein quantity was deterimed using the Pierce™

1286 BCA Protein Assay Kit (Thermo Scientific, 23225). Protein lysate samples utilized for
1287 GBP-1 detection were resolved using 4-20% Mini-PROTEAN TGX Precast Protein Gels
1288 (Bio-Rad, 4561094). Other immunoblots were performed on fixed concentration using 8-
1289 10% SDS-polyacrylamide gels. All gel transfers were performed onto nitrocellulose
1290 membranes (Fisher Scientific, 45-004-075). Nitrocellulose membranes were blocked in
1291 5% BSA/1xTBST for 1 hour at room temperature, followed by primary antibody
1292 incubation overnight on a 4ºC shaker. The following day, blots were washed with
1293 1xTBST followed by incubation with rabbit or mouse-specific horseradish peroxidase
1294 (HRP)-conjugated secondary antibodies. Signals were developed with SuperSignal
1295 West Pico PLUS Chemiluminescent Substrate (Thermo Fisher Scientific, #34577) or
1296 SuperSignal West Femto Maximum Sensitivity Substrate (Thermo Fisher Scientific,
1297 #34094). Primary antibodies used for western blotting were:
1298 Beta-Actin (13E5) Rabbit mAb, CST #4970, 1:5,000 dilution
1299 GBP-1 Rabbit Polyclonal Ab, {Thermo, PA5-23509}, 1:1,000 dilution
1300 Cas9 (S. pyogenes) (7A9-3A3) Mouse mAb, CST #14697, 1:1,000 dilution
1301 IRF-1 (D5E4) XP® Rabbit mAb, CST #8478, 1:1,000 dilution
1302 Cre Recombinase (D7L7L) XP® Rabbit mAb, CST #15036, 1:1,000 dilution
1303 GAPDH (14C10) Rabbit mAb, CST #2118, 1:5,000 dilution
1304 Stat1 (D1K9Y) Rabbit mAb, CST #14994, 1:1,000 dilution
1305 p-Stat1 (Tyr701) (58D6) Rabbit mAb #9167, 1:1,000 dilution
1306 Vinculin (E1E9V) XP® Rabbit mAb #13901, 1:5,000 dilution
1307 Anti-rabbit IgG, HRP-linked Ab, CST #7074, 1:5,000 dilution
1308 Anti-mouse IgG, HRP-linked Ab, CST #7076, 1:5,000 dilution
1309
1310 **Clinical dataset mining**
1311 Patients were stratified into IFNGR1 high and IFNGR1 low expression groups and
1312 survival curve was generated using Kaplan-Meier Plotter (KMplotter,
1313 https://www.kmplot.com). This database includes 1816 samples primarily from
1314 GSE9891 and TCGA[20]. Patient scRNA-seq RDS file was obtained from Mendeley
1315 Data[55] (https://doi.org/10.17632/rc47y6m9mp.1) and contained 14 patient samples
1316 including PBMCs, lymph nodes, primary tumor, metastasis, and malignant ascites. The

1317 RNA data was re-normalized and analyzed using the Seurat package in RStudio in
1318 similar ways to the murine scRNA-seq dataset described above.
1319
1320 **Quantitative Reverse Transcriptase (RT) PCR**
1321 The IFNγ treatment time course was performed in 12 well plates. After seeding 1.0x105
1322 cells per well, wells were treated with 100 ng/ml IFNγ for 0 hours (PBS control), 4 hours,
1323 8 hours, or 24 hours. Total cell RNA was extracted from cells using the Direct-zol RNA
1324 Miniprep kit with TriReagent (Zymo Research, R2051-A) following the manufacturer
1325 protocol. One microgram of total RNA was used for reverse transcription to synthesize
1326 single stranded cDNA using the iScript™ Reverse Transcription Supermix for RT-qPCR
1327 (Bio-Rad, 1708840). qPCR reactions were performed on a Bio-Rad CFX Opus
1328 instrument with SsoAdvanced Universal SYBR Green Supermix (Bio-Rad, 1725270).
1329 Data analysis was performed using the CFX Maestro Software. Cq values were used to
1330 calculate relative gene expression levels. In brief, calculations were based on the $2^{-\Delta\Delta CT}$
1331 method with housekeeping genes serving as internal controls and fold change was
1332 calculated by normalizing to the zero-hour treatment timepoint Cq values. Statistical
1333 analyses and plots were generated in GraphPad Prism. RT-qPCR primers used were as
1334 follows:
1335 Beta-actin (Mouse) Forward primer TM: 57.6
1336 5'- GGC TGT ATT CCC CTC CAT CG -3'
1337 Beta-actin (Mouse) Reverse primer TM: 55.9
1338 5'- CCA GTT GGT AAC AAT GCC ATG T-3'
1339 GAPDH (Mouse) Forward primer TM: 59.8
1340 5'- CAT CAC TGC CAC CCA GAA GAC TG -3'
1341 GAPDH (Mouse) Reverse primer TM: 61.6
1342 5'- ATG CCA GTG AGC TTC CCG TTC AG -3'
1343 Gbp2b (Mouse) Forward primer TM: 58.5
1344 5'- ATC TGC TCA TTG CTC AGA CTT ACT GG -3'
1345 Gbp2b (Mouse) Reverse primer TM: 57.4
1346 5'- AAG TAT TTT CTC AGC ATC ACT TCA GCC -3'
1347 Irf1 (Mouse) Forward primer TM: 60.4

1348 5’- ACC AAA TCC CAG GGC TGA TCT GG -3’
1349 Irf1 (Mouse) Reverse primer TM: 58.3
1350 5’- GAA GTT TGC CTT CCA TGT CTT GGG-3’
1351 Stat1 (Mouse) Forward primer TM: 55.1
1352 5’- GCT GCC TAT GAT GTC TCG TTT -3’
1353 Stat1 (Mouse) Reverse primer TM: 55.2
1354 5’- TGC TTT TCC GTA TGT TGT GCT -3’
1355 Marco (Mouse) Forward primer TM: 61.1
1356 5’- ATC CAC CTG ATC CTG CTC ACG G -3’
1357 Marco (Mouse) Reverse primer TM: 60.8
1358 5’- CAC TGC AGC GAG AAG AAG GGC -3’
1359 Slfn1 (Mouse) Forward primer TM: 60.9
1360 5’- AGG GAA AGG TCA AGG CTC ACA TTA AAA ATC C -3’
1361 Slfn1 (Mouse) Reverse primer TM: 60.1
1362 5’- AGG CTT CCC AAC AGA GAC ATC TGG -3’
1363
1364 **Anoikis Assay**
1365 Cancer cells ($1x10^4$) were seeded into 96-well ultra-low attachment (ULA) plates
1366 (Corning, CLS7007) to mimic anchorage-independent conditions in the peritoneal cavity
1367 environment. After 24 hours, 100 ng/ml recombinant mouse IFNγ or vehicle control
1368 (1xPBS) was added to appropriate wells. Twenty-four hours after treatment (i.e. 48hr
1369 after start of culture), CellTiter-Glo Luminescent Cell Viability Assay reagent (Promega,
1370 G7570) was applied to every assay well, and plates were incubated for 20 min at room
1371 temperature. Luminescence, indicating cellular ATP levels, was measured using a
1372 Tecan plate reader instrument and analyzed using GraphPad Prism software.
1373 For macrophage coculture experiments, $1.0x10^4$ cancer cells were seeded together with
1374 $1.0x10^4$ macrophages per well in ULA plates. Macrophages were enriched from the
1375 peritoneal cavity of wild type female mice using the MojoSort Mouse F4/80 Positive
1376 Selection Kit (BioLegend, 480170), following manufacturer’s protocol. After 48 hours of
1377 coculture, cell suspensions were harvested, pelleted, and incubated in TrypLE (Thermo
1378 Fisher Scientific, 12605028) for 10 minutes at 37 ºC to dissociate cell aggregates. Cell

1379 suspensions were passed through a 40-uM strainer before flow cytometric staining as
1380 described earlier.
1381
1382 **Colony Formation Assay**
1383 Two hundred ID8 p53$^{-/-}$ cells were plated onto 6 well plates at the start of the
1384 experiment. For wells treated with IFNγ, 100 ng/ml IFNγ was maintained throughout the
1385 7-day colony formation assay period. Wells were washed with 1xPBS, fixed with
1386 methanol, and stained with crystal violet solution (0.5% w/v) at room temperature for 20
1387 minutes. Wells were then washed with deionized water and dried overnight. Colonies
1388 were counted and quantified in GraphPad Prism.
1389
1390 **Validation of Cre-based NicheTracing**
1391 HEK293T cells were transfected with a loxp-dsRED-loxp-eGFP Cre reporter construct
1392 (Addgene # 141148) and cocultured in a 1:1 ratio with Cre.ERT2 expressing ID8 p53$^{-/-}$
1393 or E0771 cell lines in the presence or absence of 2 uM 4-hydroxytamoxifen (4-OHT,
1394 MedChemExpress, Cat # HY-16950). Seventy-two hours after plating, wells were
1395 assessed for GFP+ switched cells using a Nikon Ti2 microscope. For independent *in*
1396 *vivo* validation, E0771-Cre.ERT2 cells were injected into the retro-orbital sinus of Ai6
1397 mice. One week post injection, three consecutive tamoxifen or corn oil control
1398 treatments were performed (75 mg/kg/dose) i.p.. Two weeks post cancer cell injection,
1399 mice were euthanized, perfused intracardially, and lungs were extracted for imaging and
1400 flow cytometry analysis. For the ovarian metastasis model, tamoxifen injections were
1401 administered in five consecutive doses, two weeks post ID8-Cre.ERT2 cell i.p. injection.
1402
1403 **Bulk RNA-seq**
1404 3.0×10^5 Ifngr1-KO or sgNTC ID8 p53$^{-/-}$ cells were plated onto 6-well ULA and regular
1405 treatment plates. Recombinant IFNγ (100 ng/ml) or vehicle (1xPBS) was added to
1406 corresponding wells 24 hours post initial seeding. Cells were harvested 24 hours post
1407 IFNγ treatment. ULA samples were subjected to dead cell removal (Miltenyi Biotec, 130-
1408 090-101) and total RNA was extracted using Direct-zol RNA Miniprep kit with
1409 TriReagent (Zymo Research, R2051-A) following the manufacturer protocol. Purified

RNA was subjected to library preparation. In brief, mRNA was purified using poly-T oligo magnetic beads, fragmented, and reverse transcribed. Resulting cDNA was subjected to amplification and indexing. Final libraries were sequenced on a NovaSeq-X instrument. Raw reads were trimmed and aligned to the mouse reference genome (mm10). Following transcript level quantification, subsequent count matrices were analyzed in RStudio. DESeq2 was used for downstream analysis and variance-stabilized counts (VSTs) were used for PCA and visualization. Pathway analysis (Hallmark, Reactome, Go Biological Processes) was conducted through the clusterProfiler R package.

Data and Resource Availability

scRNA-seq datasets with LARRY barcode and HTO multiplexing was deposited at GEO: GSE302619 (ovarian) and GSE309120 (lung) and will be made publicly available upon publishing. Reviewer access tokens for the datasets presented here are: qvevaiacnnarbwr (ovarian) and obyficmwzdmnnkh (lung). Human scRNA-seq data has been published elsewhere and is publicly available: GSE14764. Code and any additional information required to reanalyze the data reported here can be requested from the lead contact.

Declaration of generative AI and AI-assisted technologies in the writing process

During the preparation of this work the author(s) used ChatGPT in order to improve writing clarity. After using this tool/service, the author(s) reviewed and edited the content as needed and take(s) full responsibility for the content of the publication.

REFERENCES:

1. Gerstberger, S., Jiang, Q., and Ganesh, K. (2023). Metastasis. Cell *186*, 1564–1579. https://doi.org/10.1016/j.cell.2023.03.003.

2. Ritch, S.J., and Telleria, C.M. (2022). The Transcoelomic Ecosystem and Epithelial Ovarian Cancer Dissemination. Front. Endocrinol. *13*, 886533. https://doi.org/10.3389/fendo.2022.886533.

3. Motohara, T., Masuda, K., Morotti, M., Zheng, Y., El-Sahhar, S., Chong, K.Y., Wietek, N., Alsaadi, A., Carrami, E.M., Hu, Z., et al. (2019). An evolving story of the metastatic voyage of ovarian cancer cells: cellular and molecular orchestration of the adipose-rich metastatic microenvironment. Oncogene *38*, 2885–2898. https://doi.org/10.1038/s41388-018-0637-x.

4. Almeida-Nunes, D.L., Mendes-Frias, A., Silvestre, R., Dinis-Oliveira, R.J., and Ricardo, S. (2022). Immune Tumor Microenvironment in Ovarian Cancer Ascites. Int. J. Mol. Sci. *23*, 10692. https://doi.org/10.3390/ijms231810692.

5. Lane, D., Matte, I., Garde-Granger, P., Bessette, P., and Piché, A. (2018). Ascites IL-10 Promotes Ovarian Cancer Cell Migration. Cancer Microenviron. *11*, 115–124. https://doi.org/10.1007/s12307-018-0215-3.

6. Mustea, A., Pirvulescu, C., Könsgen, D., Braicu, E.I., Yuan, S., Sun, P., Lichtenegger, W., and Sehouli, J. (2008). Decreased IL-1 RA concentration in ascites is associated with a significant improvement in overall survival in ovarian cancer. Cytokine *42*, 77–84. https://doi.org/10.1016/j.cyto.2008.01.011.

7. Ahmed, N., and Stenvers, K. (2013). Getting to Know Ovarian Cancer Ascites: Opportunities for Targeted Therapy-Based Translational Research. Front. Oncol. *3*. https://doi.org/10.3389/fonc.2013.00256.

8. Lineage tracing on transcriptional landscapes links state to fate during differentiation | Science (2025). https://www.science.org/doi/10.1126/science.aaw3381.

9. Dasgupta, A., Lim, A.R., and Ghajar, C.M. (2017). Circulating and disseminated tumor cells: harbingers or initiators of metastasis? Mol. Oncol. *11*, 40–61. https://doi.org/10.1002/1878-0261.12022.

10. Borcherding, N., Vishwakarma, A., Voigt, A.P., Bellizzi, A., Kaplan, J., Nepple, K., Salem, A.K., Jenkins, R.W., Zakharia, Y., and Zhang, W. (2021). Mapping the immune environment in clear cell renal carcinoma by single-cell genomics. Commun. Biol. *4*, 122. https://doi.org/10.1038/s42003-020-01625-6.

11. Cellular barcoding to decipher clonal dynamics in disease | Science (2025). https://www.science.org/doi/10.1126/science.abm5874?url_ver=Z39.88-2003&rfr_id=ori:rid:crossref.org&rfr_dat=cr_pub%20%200pubmed.

12. CellRank for directed single-cell fate mapping | Nature Methods (2025). https://www.nature.com/articles/s41592-021-01346-6.

13. Yu, G., Wang, L.-G., Han, Y., and He, Q.-Y. (2012). clusterProfiler: an R Package for Comparing Biological Themes Among Gene Clusters. OMICS J. Integr. Biol. *16*, 284–287. https://doi.org/10.1089/omi.2011.0118.

14. Bahrami, S., and Drabløs, F. (2016). Gene regulation in the immediate-early response process. Adv. Biol. Regul. *62*, 37–49. https://doi.org/10.1016/j.jbior.2016.05.001.

15. Koivisto, E., Acosta, A.J., Moilanen, A.-M., Tokola, H., Aro, J., Pennanen, H., Säkkinen, H., Kaikkonen, L., Ruskoaho, H., and Rysä, J. (2014). Characterization of the Regulatory Mechanisms of Activating Transcription Factor 3 by Hypertrophic Stimuli in Rat Cardiomyocytes. PLOS ONE *9*, e105168. https://doi.org/10.1371/journal.pone.0105168.

16. Zhao, J., Peng, H., Gao, J., Nong, A., Hua, H., Yang, S., Chen, L., Wu, X., Zhang, H., and Wang, J. (2021). Current insights into the expression and functions of tumor-derived immunoglobulins. Cell Death Discov. *7*, 148. https://doi.org/10.1038/s41420-021-00550-9.

17. Mehta, A., and Merkel, O.M. (2020). Immunogenicity of Cas9 Protein. J. Pharm. Sci. *109*, 62–67. https://doi.org/10.1016/j.xphs.2019.10.003.

18. Li, W., Xu, H., Xiao, T., Cong, L., Love, M.I., Zhang, F., Irizarry, R.A., Liu, J.S., Brown, M., and Liu, X.S. (2014). MAGeCK enables robust identification of essential genes from genome-scale CRISPR/Cas9 knockout screens. Genome Biol. *15*, 554. https://doi.org/10.1186/s13059-014-0554-4.

19. Shultz, D.B., Sandhya Rani, M.R., Fuller, J.D., Ransohoff, R.M., and Stark, G.R. (2009). Roles of IKK-β, IRF1, and p65 in the Activation of Chemokine Genes by Interferon-γ. J. Interferon Cytokine Res. *29*, 817–824. https://doi.org/10.1089/jir.2009.0034.

20. Győrffy, B. (2023). Discovery and ranking of the most robust prognostic biomarkers in serous ovarian cancer. GeroScience *45*, 1889–1898. https://doi.org/10.1007/s11357-023-00742-4.

21. Rouette, A., Trofimov, A., Haberl, D., Boucher, G., Lavallée, V.-P., D'Angelo, G., Hébert, J., Sauvageau, G., Lemieux, S., and Perreault, C. (2016). Expression of immunoproteasome genes is regulated by cell-intrinsic and –extrinsic factors in human cancers. Sci. Rep. *6*, 34019. https://doi.org/10.1038/srep34019.

22. Ma, X., Li, Y., Wang, D., Niu, J., Li, Q., Chen, Y., Wang, M., Wen, J., Liao, C., Wang, N., et al. (2025). PSMB10 maintains the stemness of chemotherapeutic drug-resistant leukemia cells by inhibiting senescence and cytotoxic T lymphocyte-mediated killing in a ubiquitinated degradation manner. J. Exp. Clin. Cancer Res. *44*, 170. https://doi.org/10.1186/s13046-025-03420-9.

23. Barbarulo, A., Iansante, V., Chaidos, A., Naresh, K., Rahemtulla, A., Franzoso, G., Karadimitris, A., Haskard, D.O., Papa, S., and Bubici, C. (2013). Poly(ADP-ribose) polymerase family member 14 (PARP14) is a novel effector of the JNK2-dependent pro-survival signal in multiple myeloma. Oncogene *32*, 4231–4242. https://doi.org/10.1038/onc.2012.448.

24. Escors, D., Gato-Cañas, M., Zuazo, M., Arasanz, H., García-Granda, M.J., Vera, R., and Kochan, G. (2018). The intracellular signalosome of PD-L1 in cancer cells. Signal Transduct. Target. Ther. *3*, 26. https://doi.org/10.1038/s41392-018-0022-9.

25. Jin, S., Guerrero-Juarez, C.F., Zhang, L., Chang, I., Ramos, R., Kuan, C.-H., Myung, P., Plikus, M.V., and Nie, Q. (2021). Inference and analysis of cell-cell communication using CellChat. Nat. Commun. *12*, 1088. https://doi.org/10.1038/s41467-021-21246-9.

26. Chen, S., Saeed, A.F.U.H., Liu, Q., Jiang, Q., Xu, H., Xiao, G.G., Rao, L., and Duo, Y. (2023). Macrophages in immunoregulation and therapeutics. Signal Transduct. Target. Ther. *8*, 207. https://doi.org/10.1038/s41392-023-01452-1.

27. Ahmed, I., and Ismail, N. (2020). M1 and M2 Macrophages Polarization via mTORC1 Influences Innate Immunity and Outcome of Ehrlichia Infection. J. Cell. Immunol. *2*, 108–115. https://doi.org/10.33696/immunology.2.029.

28. O'Carroll, C., Fagan, A., Shanahan, F., and Carmody, R.J. (2014). Identification of a Unique Hybrid Macrophage-Polarization State following Recovery from Lipopolysaccharide Tolerance. J. Immunol. *192*, 427–436. https://doi.org/10.4049/jimmunol.1301722.

29. Patterson, M.T., Firulyova, M.M., Xu, Y., Hillman, H., Bishop, C., Zhu, A., Hickok, G.H., Schrank, P.R., Ronayne, C.E., Caillot, Z., et al. (2023). Trem2 promotes foamy macrophage lipid uptake and survival in atherosclerosis. Nat. Cardiovasc. Res. *2*, 1015–1031. https://doi.org/10.1038/s44161-023-00354-3.

30. Binnewies, M., Pollack, J.L., Rudolph, J., Dash, S., Abushawish, M., Lee, T., Jahchan, N.S., Canaday, P., Lu, E., Norng, M., et al. (2021). Targeting TREM2 on tumor-associated macrophages enhances immunotherapy. Cell Rep. *37*, 109844. https://doi.org/10.1016/j.celrep.2021.109844.

31. Park, M.D., Reyes-Torres, I., LeBerichel, J., Hamon, P., LaMarche, N.M., Hegde, S., Belabed, M., Troncoso, L., Grout, J.A., Magen, A., et al. (2023). TREM2 macrophages drive NK cell paucity and dysfunction in lung cancer. Nat. Immunol. *24*, 792–801. https://doi.org/10.1038/s41590-023-01475-4.

32. Iyer, S., Zhang, S., Yucel, S., Horn, H., Smith, S.G., Reinhardt, F., Hoefsmit, E., Assatova, B., Casado, J., Meinsohn, M.-C., et al. (2021). Genetically Defined Syngeneic Mouse Models of Ovarian Cancer as Tools for the Discovery of Combination Immunotherapy. Cancer Discov. *11*, 384–407. https://doi.org/10.1158/2159-8290.CD-20-0818.

33. Zheng, X., Wang, X., Cheng, X., Liu, Z., Yin, Y., Li, X., Huang, Z., Wang, Z., Guo, W., Ginhoux, F., et al. (2023). Single-cell analyses implicate ascites in remodeling the ecosystems of primary and metastatic tumors in ovarian cancer. Nat. Cancer *4*, 1138–1156. https://doi.org/10.1038/s43018-023-00599-8.

34. Patras, L., Shaashua, L., Matei, I., and Lyden, D. (2023). Immune determinants of the pre-metastatic niche. Cancer Cell *41*, 546–572. https://doi.org/10.1016/j.ccell.2023.02.018.

35. Peinado, H., Zhang, H., Matei, I.R., Costa-Silva, B., Hoshino, A., Rodrigues, G., Psaila, B., Kaplan, R.N., Bromberg, J.F., Kang, Y., et al. (2017). Pre-metastatic niches: organ-specific homes for metastases. Nat. Rev. Cancer *17*, 302–317. https://doi.org/10.1038/nrc.2017.6.

36. Hershey, B.J., Barozzi, S., Orsenigo, F., Pompei, S., Iannelli, F., Kamrad, S., Matafora, V., Pisati, F., Calabrese, L., Fragale, G., et al. (2023). Clonal cooperation through soluble metabolite exchange facilitates metastatic outgrowth by modulating Allee effect. Sci. Adv. *9*, eadh4184. https://doi.org/10.1126/sciadv.adh4184.

37. Śliwa, A., Szczerba, A., Pięta, P.P., Białas, P., Lorek, J., Nowak-Markwitz, E., and Jankowska, A. (2024). A Recipe for Successful Metastasis: Transition and Migratory Modes of Ovarian Cancer Cells. Cancers *16*, 783. https://doi.org/10.3390/cancers16040783.

38. Schrijver, W.A.M.E., Selenica, P., Lee, J.Y., Ng, C.K.Y., Burke, K.A., Piscuoglio, S., Berman, S.H., Reis-Filho, J.S., Weigelt, B., van Diest, P.J., et al. (2018). Mutation Profiling of Key Cancer Genes in Primary Breast Cancers and Their Distant Metastases. Cancer Res. *78*, 3112–3121. https://doi.org/10.1158/0008-5472.CAN-17-2310.

39. Müller, V., and Pantel, K. (2004). Bone marrow micrometastases and circulating tumor cells: current aspects and future perspectives. Breast Cancer Res. *6*, 258–261. https://doi.org/10.1186/bcr942.

40. Sänger, N., Effenberger, K.E., Riethdorf, S., Van Haasteren, V., Gauwerky, J., Wiegratz, I., Strebhardt, K., Kaufmann, M., and Pantel, K. (2011). Disseminated tumor cells in the bone marrow of patients with ductal carcinoma in situ. Int. J. Cancer *129*, 2522–2526. https://doi.org/10.1002/ijc.25895.

41. Wawrzyniak, P., and Hartman, M.L. (2025). Dual role of interferon-gamma in the response of melanoma patients to immunotherapy with immune checkpoint inhibitors. Mol. Cancer *24*, 89. https://doi.org/10.1186/s12943-025-02294-x.

42. Remsik, J., Tong, X., Kunes, R.Z., Li, M.J., Estrera, R., Snyder, J., Thomson, C., Osman, A.M., Chabot, K., Sener, U.T., et al. (2025). Interferon-γ orchestrates leptomeningeal anti-tumour response. Nature, 1–10. https://doi.org/10.1038/s41586-025-09012-z.

43. Jorgovanovic, D., Song, M., Wang, L., and Zhang, Y. (2020). Roles of IFN-γ in tumor progression and regression: a review. Biomark. Res. *8*, 49. https://doi.org/10.1186/s40364-020-00228-x.

1590 44. Zheng, H., Guan, X., Meng, X., Tong, Y., Wang, Y., Xie, S., Guo, L., and Lu, R.
1591 (2023). IFN-γ in ovarian tumor microenvironment upregulates HLA-E expression and
1592 predicts a poor prognosis. J. Ovarian Res. *16*, 229. https://doi.org/10.1186/s13048-
1593 023-01286-z.

1594 45. Reddy, S.U., Sadia, F.Z., Vancura, A., and Vancurova, I. (2024). IFNγ-Induced Bcl3,
1595 PD-L1 and IL-8 Signaling in Ovarian Cancer: Mechanisms and Clinical Significance.
1596 Cancers *16*, 2676. https://doi.org/10.3390/cancers16152676.

1597 46. Murphy, B., Miyamoto, T., Manning, B.S., Mirji, G., Ugolini, A., Kannan, T., Hamada,
1598 K., Zhu, Y.P., Claiborne, D.T., Huang, L., et al. (2024). Myeloid activation clears
1599 ascites and reveals IL27-dependent regression of metastatic ovarian cancer. J. Exp.
1600 Med. *221*, e20231967. https://doi.org/10.1084/jem.20231967.

1601 47. Ye, Z., Ai, X., Zhao, L., Fei, F., Wang, P., and Zhou, S. (2021). Phenotypic plasticity
1602 of myeloid cells in glioblastoma development, progression, and therapeutics.
1603 Oncogene *40*, 6059–6070. https://doi.org/10.1038/s41388-021-02010-1.

1604 48. Schol, P., Elsas, M.J. van, Middelburg, J., Twilhaar, M.K.N., Hall, T. van, Sluis, T.C.
1605 van der, and Burg, S.H. van der (2024). Myeloid effector cells in cancer. Cancer Cell
1606 *42*, 1997–2014. https://doi.org/10.1016/j.ccell.2024.11.002.

1607 49. Guilliams, M., and Svedberg, F.R. (2021). Does tissue imprinting restrict
1608 macrophage plasticity? Nat. Immunol. *22*, 118–127. https://doi.org/10.1038/s41590-
1609 020-00849-2.

1610 50. Yarilina, A., Park-Min, K.-H., Antoniv, T., Hu, X., and Ivashkiv, L.B. (2008). TNF
1611 activates an IRF1-dependent autocrine loop leading to sustained expression of
1612 chemokines and STAT1-dependent type I interferon–response genes. Nat. Immunol.
1613 *9*, 378–387. https://doi.org/10.1038/ni1576.

1614 51. Toney, N.J., Opdenaker, L.M., Frerichs, L., Modarai, S.R., Ma, A., Archinal, H., Ajayi,
1615 G.O., and Sims-Mourtada, J. (2025). B cells enhance IL-1 beta driven invasiveness
1616 in triple negative breast cancer. Sci. Rep. *15*, 2211. https://doi.org/10.1038/s41598-
1617 025-86064-1.

1618 52. Luo, J.-L., Kamata, H., and Karin, M. (2005). IKK/NF-κB signaling: balancing life and
1619 death – a new approach to cancer therapy. J. Clin. Invest. *115*, 2625–2632.
1620 https://doi.org/10.1172/JCI26322.

1621 53. Horowitz, J.C., Lee, D.Y., Waghray, M., Keshamouni, V.G., Thomas, P.E., Zhang, H.,
1622 Cui, Z., and Thannickal, V.J. (2004). Activation of the pro-survival
1623 phosphatidylinositol 3-kinase/AKT pathway by transforming growth factor-beta1 in
1624 mesenchymal cells is mediated by p38 MAPK-dependent induction of an autocrine
1625 growth factor. J. Biol. Chem. *279*, 1359–1367.
1626 https://doi.org/10.1074/jbc.M306248200.

54. Xu, Y., Tabe, Y., Jin, L., Watt, J., McQueen, T., Ohsaka, A., Andreeff, M., and Konopleva, M. (2008). TGF-beta receptor kinase inhibitor LY2109761 reverses the anti-apoptotic effects of TGF-beta1 in myelo-monocytic leukaemic cells co-cultured with stromal cells. Br. J. Haematol. *142*, 192–201. https://doi.org/10.1111/j.1365-2141.2008.07130.x.

55. Wang, X., and Zheng, X. (2022). scRNA-seq data in ovarian cancer. *1*. https://doi.org/10.17632/rc47y6m9mp.1.

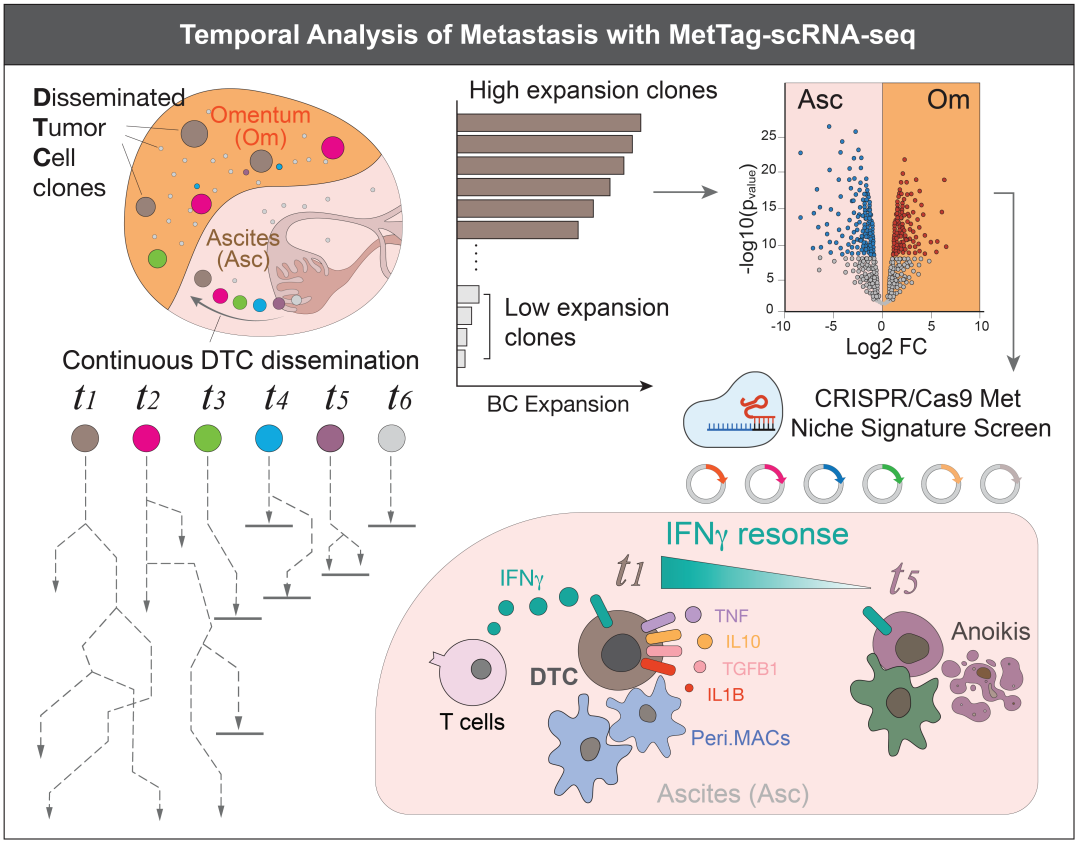

Graphical abstract

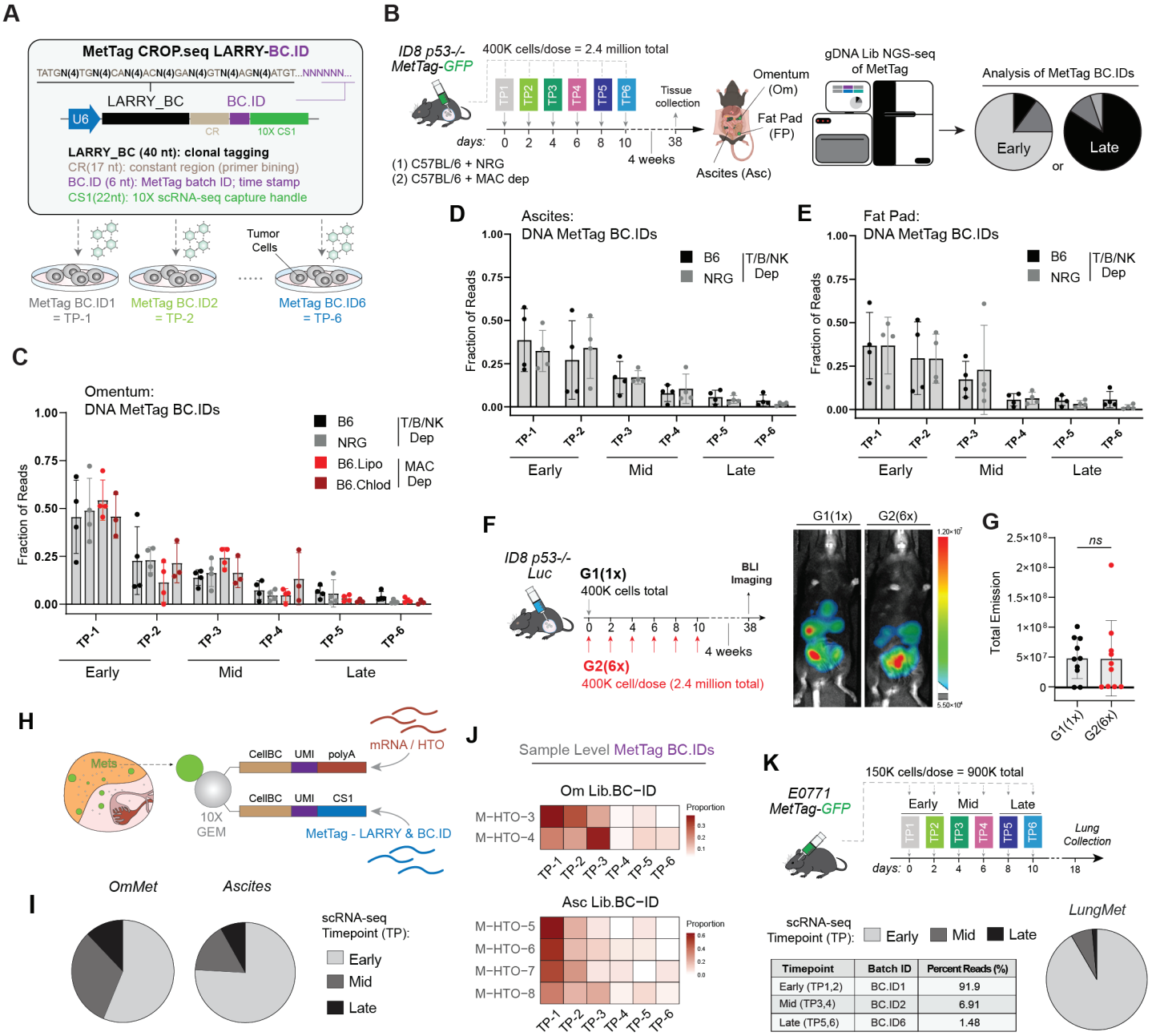

Timepoint	Batch ID	Percent Reads (%)
Early (TP1,2)	BC.ID1	91.9
Mid (TP3,4)	BC.ID2	6.91
Late (TP5,6)	BC.ID6	1.48

Figure 1: Tracking Clonal Lineage in Ovarian Cancer Metastasis
(**A**) Schematic depicting main elements of the MetTag library barcoding construct. (**B**) Schematic of injection and tissue collection timeline for the staggered injection experimental model using MetTag-barcoded ID8 ovarian cell lines. Schematic was partially created with BioRender.com. (**C**) Genomic DNA (gDNA)-level barcode distributions in the omentum graphed as frequency under WT, NRG, and MAC depletion conditions. (**D-E**) gDNA-level barcode distributions in ascites and pelvic fat pads under WT and NRG conditions. In (C-E) panels, BC.ID1 = TP-1, BC.ID2 = TP-2, BC.ID3 = TP-3, BC.ID4 = TP-4, BC.ID5 = TP-5, BC.ID6 = TP-6 for clarity. (**F**) Injection schema for comparing one-time (400,000 total, n = 10) cell dose and fractionated (2,400,000 total, n = 10) cell injections (left) and representative BLI images at endpoint (right). (**G**) Bar graph depicting total flux emission in each group at experimental endpoint. (**H**) Schematic of scRNA-seq experiment conducted using a reversed BC.ID injection order. LARRY barcodes are readily captured by Chromium 10x Feature Barcoding. (**I**) Pie charts of RNA-level barcode frequencies in each location grouped as early (BC.ID5, BC.ID6), mid (BC.ID4, BC.ID3), and late (BC.ID2, BC.ID1). (**J**) Heatmap of sample level barcode frequencies, BC.ID6 = TP-1, BC.ID5 = TP-2, BC.ID4 = TP-3, BC.ID3 = TP-4, BC.ID2 = TP-5, BC.ID1 = TP-6. (**K**) Schematic (top) and MetTag BC.ID distribution (bottom) for independent TNBC lung metastasis model depicting enrichment of scRNA-seq derived early TP DTCs in the metastatic lung at endpoint. Data in Figure 1G was analyzed using a two-tailed Student's t test and graphed as mean with standard deviation (SD).

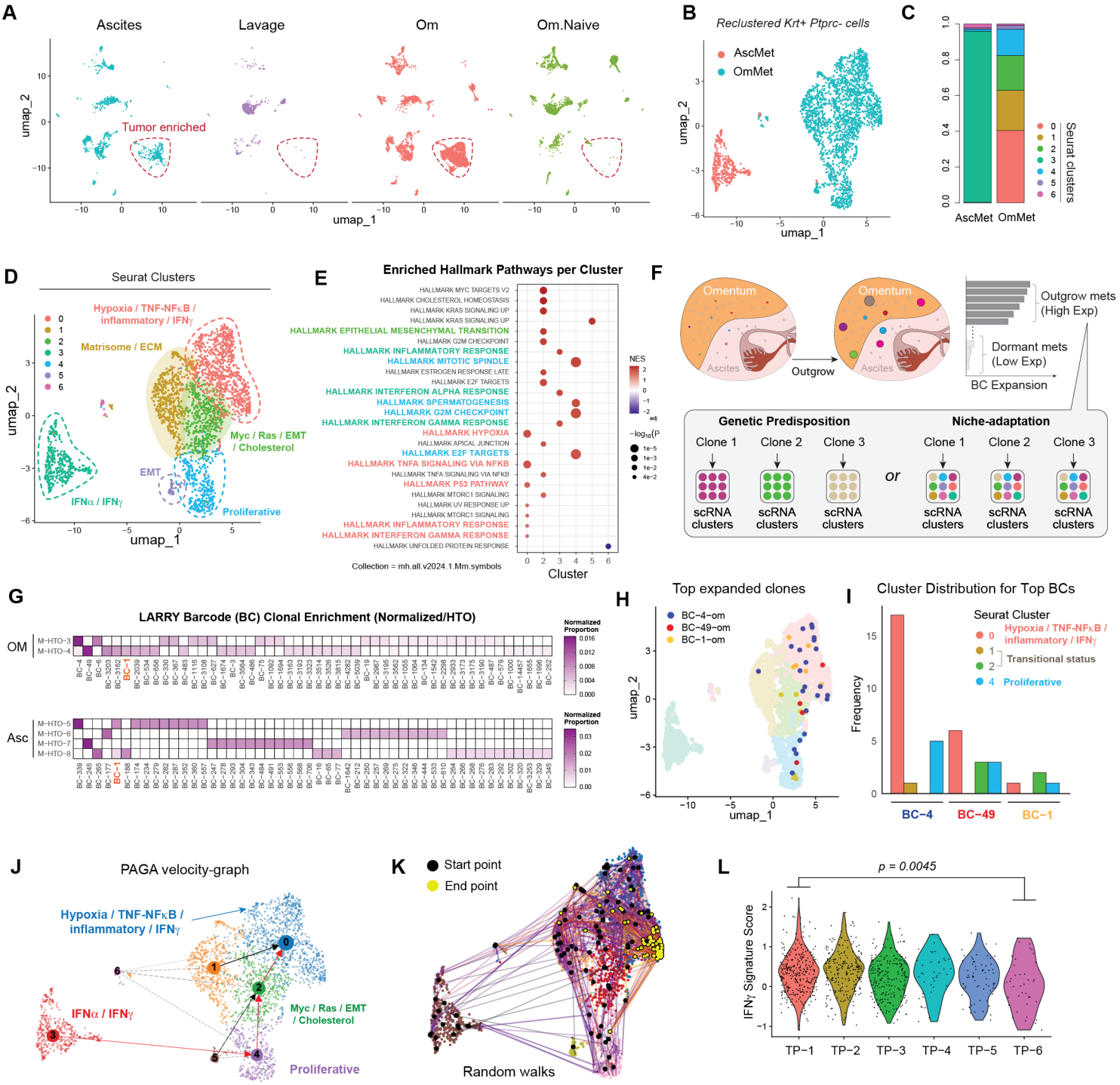

Figure 2: Clonal Analysis Reveals Shared Evolutionary Path Towards Inflammatory Signature
(**A**) Split UMAP depicting cluster distributions across the four experimental conditions and identifying cancer cell-enriched clusters in ascites and omentum. (**B**) Reclustered cancer cell UMAP colored by the two metastasis-bearing anatomical locations. (**C**) Stacked bar chart depicting the frequency of Seurat subclusters within each metastatic location. (**D**) Seurat cluster UMAP of reclustered cancer cells with transcriptional program labels. (**E**) Dot plot depicting Hallmark pathways across all subclusters used to define each cluster subset gene program in (D). (**F**) Schematic representation of the possible outcomes of LARRY clonal analysis based on transcriptome patterns of enriched clones. (**G**) Heatmap of normalized clonal LARRY barcode counts across the two anatomical locations and individual mice (HTOs). (**H**) UMAP overlay of top 3 expanded clones in the omentum. (**I**) Bar chart depicting the relative subcluster proportions present in each of the top 3 barcode clones. (**J**) scVelo-generated PAGA velocity graph indicating trajectory arrows and inferred cluster lineage. (**K**) scVelo and CellRank-based simulated path from start to endpoint clusters. (**L**) Violin plot depicting RNA-level contribution of each timepoint to the IFN-gamma signature. Data in Figure 2L was analyzed by first defining the IFN-gamma signature using canonical mouse genes, followed by directly applying the wilcox.test() function in Seurat to compare TP-1 and TP-6 expression.

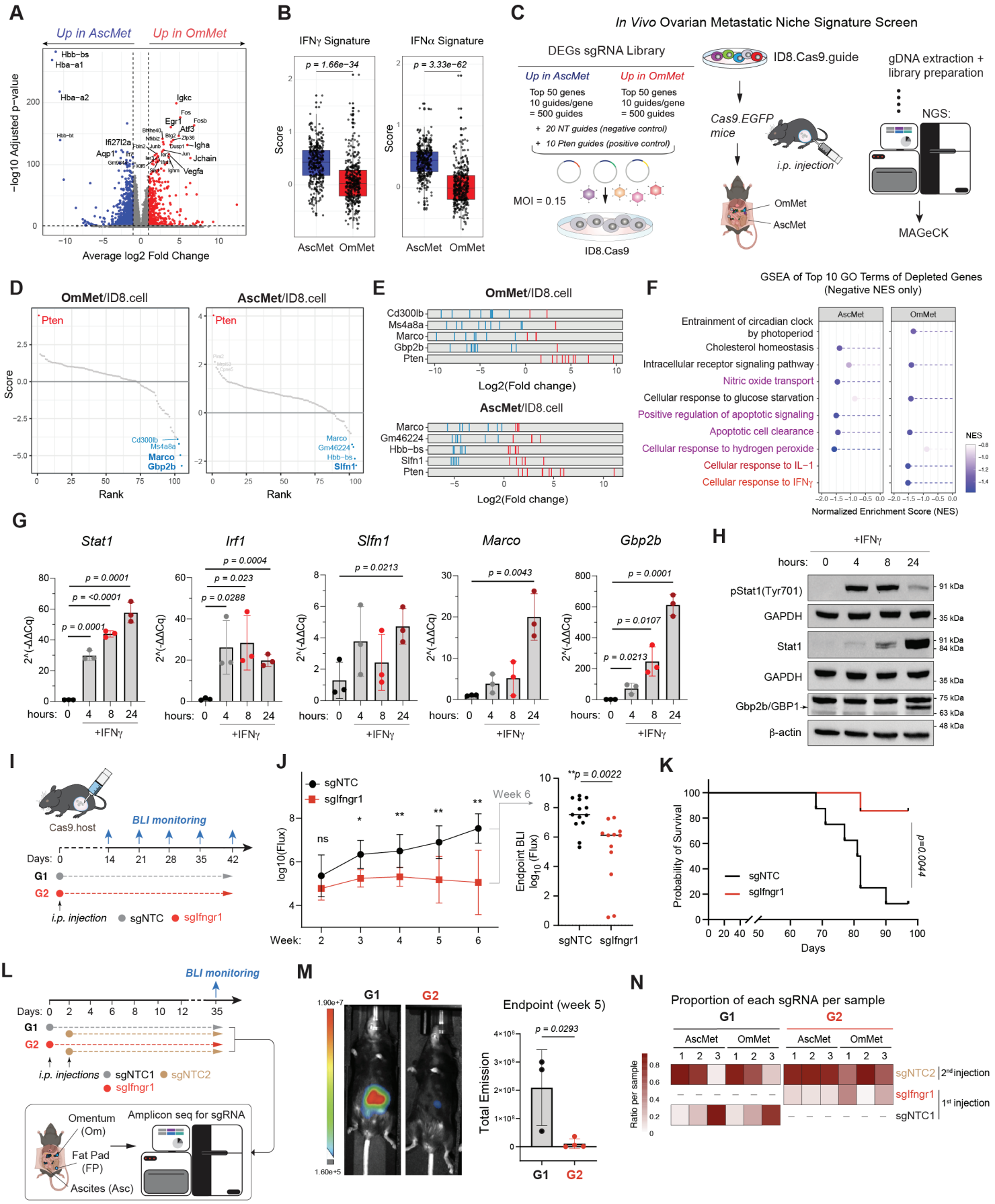
A
Up in AscMet
Up in OmMet
−log10 Adjusted p-value
Average log2 Fold Change
Hbb−bs
Hba−a1
Hba−a2
Igkc
Egr1
Atf3
Fosb
Ifi27l2a
Aqp1
Igha
Jchain
Vegfa
B
IFNγ Signature
IFNα Signature
p = 1.66e−34
p = 3.33e−62
Score
AscMet
OmMet
C
In Vivo Ovarian Metastatic Niche Signature Screen
DEGs sgRNA Library
Up in AscMet
Up in OmMet
Top 50 genes
10 guides/gene
= 500 guides
+ 20 NT guides (negative control)
+ 10 Pten guides (positive control)
MOI = 0.15
ID8.Cas9
ID8.Cas9.guide
Cas9.EGFP mice
i.p. injection
OmMet
AscMet
gDNA extraction + library preparation
NGS:
MAGeCK
D
OmMet/ID8.cell
AscMet/ID8.cell
Pten
Cd300lb
Ms4a8a
Marco
Gbp2b
Gm46224
Hbb−bs
Slfn1
Score
Rank
E
OmMet/ID8.cell
AscMet/ID8.cell
Cd300lb
Ms4a8a
Marco
Gbp2b
Pten
Gm46224
Hbb−bs
Slfn1
Log2(Fold change)
F
GSEA of Top 10 GO Terms of Depleted Genes (Negative NES only)
AscMet
OmMet
Entrainment of circadian clock by photoperiod
Cholesterol homeostasis
Intracellular receptor signaling pathway
Nitric oxide transport
Cellular response to glucose starvation
Positive regulation of apoptotic signaling
Apoptotic cell clearance
Cellular response to hydrogen peroxide
Cellular response to IL−1
Cellular response to IFNγ
NES
Normalized Enrichment Score (NES)
G
Stat1
Irf1
Slfn1
Marco
Gbp2b
2^(-ΔΔCq)
hours: 0 4 8 24
+IFNγ
p = 0.0001
p = <0.0001
p = 0.0004
p = 0.023
p = 0.0288
p = 0.0213
p = 0.0043
p = 0.0107
H
+IFNγ
hours: 0 4 8 24
pStat1(Tyr701)
GAPDH
Stat1
Gbp2b/GBP1
β-actin
91 kDa
35 kDa
84 kDa
75 kDa
63 kDa
48 kDa
I
Cas9.host
BLI monitoring
Days: 0 14 21 28 35 42
G1
G2
i.p. injection
sgNTC
sgIfngr1
J
sgNTC
sgIfngr1
log10(Flux)
Week: 2 3 4 5 6
ns
Week 6
Endpoint BLI log10 (Flux)
**p = 0.0022
K
Probability of Survival
Days
sgNTC
sgIfngr1
p=0.0044
L
BLI monitoring
Days: 0 2 4 6 8 10 12 35
G1
G2
i.p. injections
sgNTC1
sgNTC2
sgIfngr1
Omentum (Om)
Fat Pad (FP)
Ascites (Asc)
Amplicon seq for sgRNA
M
G1
G2
1.90e+7
1.60e+5
Endpoint (week 5)
p = 0.0293
Total Emission
N
Proportion of each sgRNA per sample
G1
G2
AscMet
OmMet
Ratio per sample
sgNTC2
sgIfngr1
sgNTC1
2nd injection
1st injection

Figure 3: Activation of IFNγ Response in Ascites is Necessary for Successful Omental Colonization
(**A**) DEG-based volcano plot of gene expression differences between OmMet and AscMet, where threshold for significance was defined at p <0.05 and log2FC < -1.0 for downregulation or >1.0 for upregulation. (**B**) Boxplots comparing IFN signature modules between AscMet and OmMet. (**C**) Schematic describing in vivo ovarian metastatic niche signature screen. Partially created with BioRender.com. (**D**) *In vivo* CRISPR screen RankView plots for all 100 genes generated using MAGeCKFlute. OmMet (n=5) and AscMet (n=4) samples were compared to the original pool of ID8 cells. (**E**) Ranks of individual sgRNAs targeting positive control Pten and depleted genes. (**F**) Lollipop plot of depleted pathways associated with depleted genes in Fig. 3E. (**G**) IFNγ treatment time course qPCR plots of select CRISPR hits and positive controls. (**H**) IFNγ treatment time course western blot probing for Stat1/pStat1 and GBP1. (**I**) Schematic of in vivo experimental metastasis study comparing sgNTC and sgIFNGR1.g1 groups. (**J**) Time course log10-transformed total emission/flux values (left). Two independent groups pooled; cohort 1 NTC; n = 8, KO; n = 7; cohort 2 NTC; n = 5, KO; n = 5. log10-transformed flux plot for week six with p value (right). (**K**) Kaplan Meier survival curve generated for cohort 1. (**L**) Experimental schematic for staggered sgIfngr1 (*n = 4*) or sgNTC1 (*n = 3*) followed by sgNTC2-cell injection. (**M**) Representative endpoint BLI images of metastasis bearing mice in each group (left) and endpoint BLI quantification comparing tumor burden between sgIfngr1 and sgNTC first injection (right). (**N**) Heatmap showing enrichment of first DTC seed - either sgNTC1 or sgIfngr1 - and 2nd DTC seed, sgNTC2. DEG data in Figure 3A was analyzed using the FindMarkers() function. Data in Figure 3B was analyzed by first defining custom IFN signatures, followed by applying wilcox.test() in Seurat to compare module scores between AscMet and OmMet. CRISPR screen related data (3D-3F) was analyzed using MAGeCK and MAGeCKFlute. Data in 3G, 3J, 3K, and 3M was analyzed and graphed in Prism. 3G, SJ, and 3M were analyzed using a standard t test; 3G and 3M data was plotted as mean with SD, while 3J was plotted as median. Survival data in 3K was computed using a standard log-rank test.

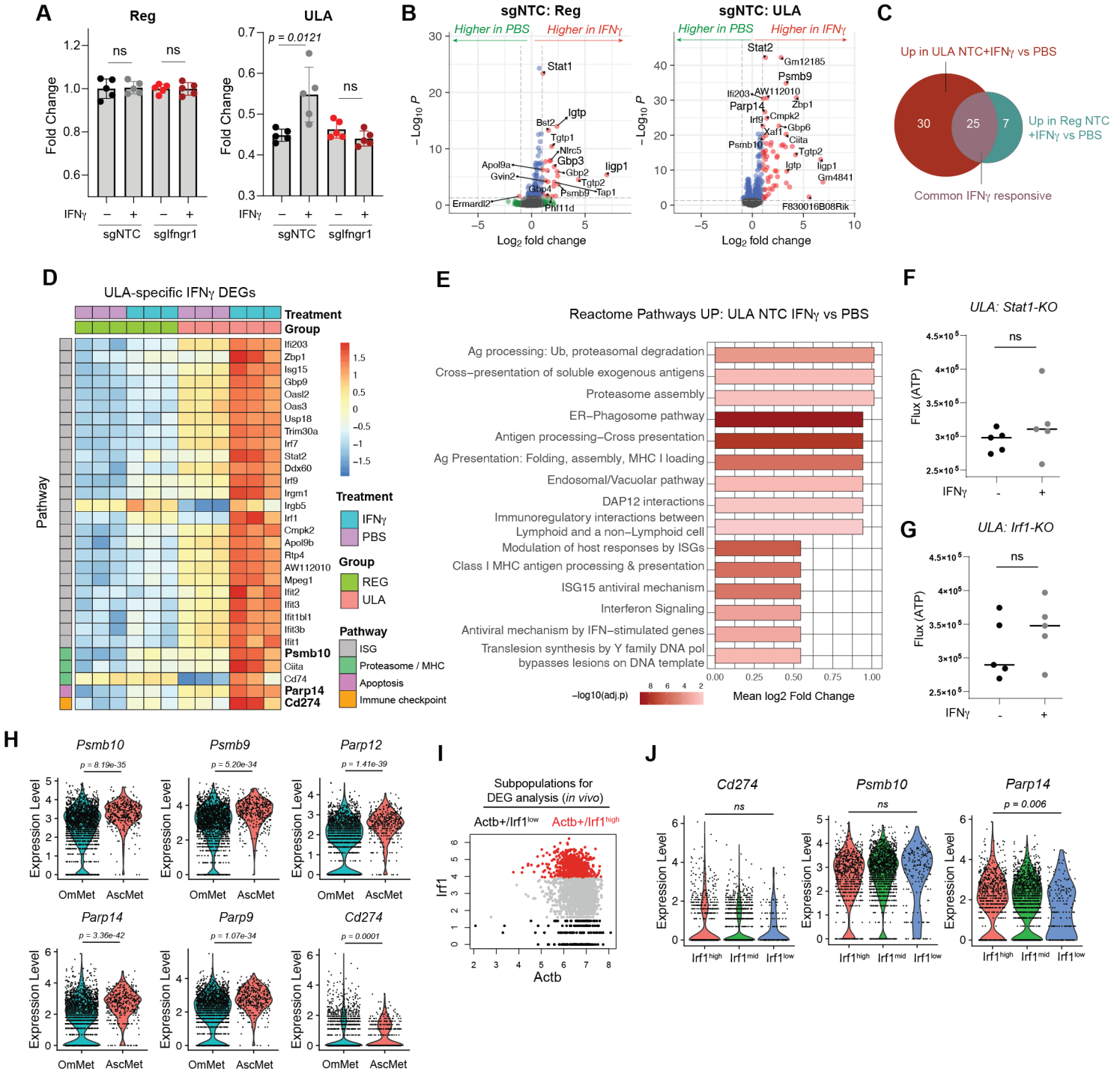

Figure 4: IFNγ Response Mediates Resistance to Anoikis and Activates Pro-survival Programs
(**A**) Cell-Titer Glo (CTG) assay luminescence values graphed as fold change for regular culture conditions (left) and ultra-low attachment (ULA) conditions (right), with and without IFNγ treatment. (**B**) Volcano plots generated from bulk RNA-seq depicting top DEGs between sgNTC (wild type) cells under regular culture conditions with or without IFNγ treatment (left) and under ULA conditions with and without IFNγ treatment (right). (**C**) Venn diagram showing 25 overlapping and 30 unique upregulated genes in sgNTC cells treated with IFNγ under ULA conditions. (**D**) Heatmap of vst-normalized gene counts for ULA-specific upregulated genes. (**E**) Bar plot depicting top 15 Reactome pathways upregulated under ULA conditions in cells treated with IFNγ. (**F-G**) CTG flux dot plots for Stat1-KO (F) and Irf1-KO (G) cells under ultra-low attachment, with or without IFNγ treatment. (**H**) Violin plots comparing expression level of immunoproteasome (Psmb10, Psmb9), DNA repair/apoptosis (Parp12, Parp14, Parp9), and immune checkpoint (Cd274) levels between OmMet and AscMet. (**I**) scRNA-seq based gating strategy used to identify Irf1^{high} and Irf1^{low} cells for module scoring. (**J**) Violin plots comparing expression level of *Cd274* (left), *Psmb10* (middle), and *Parp14* (right) between Irf1^{high} and Irf1^{low} cells. Fold change in F4A was determined by normalizing each cell line's CTG value to the regular attachment, without IFNγ treatment.CTG assay luminescence data (4A) was graphed as mean and SD, data in 4F and 4G was graphed as median values. scRNA-seq based transcript expression levels were compared between Irf1^{high} and Irf1^{low} cells and OmMet/AscMet cells by applying the wilcox.test() function in Seurat. RNA-seq data was analyzed using DESeq2 and visualized as variance-stabilized counts.

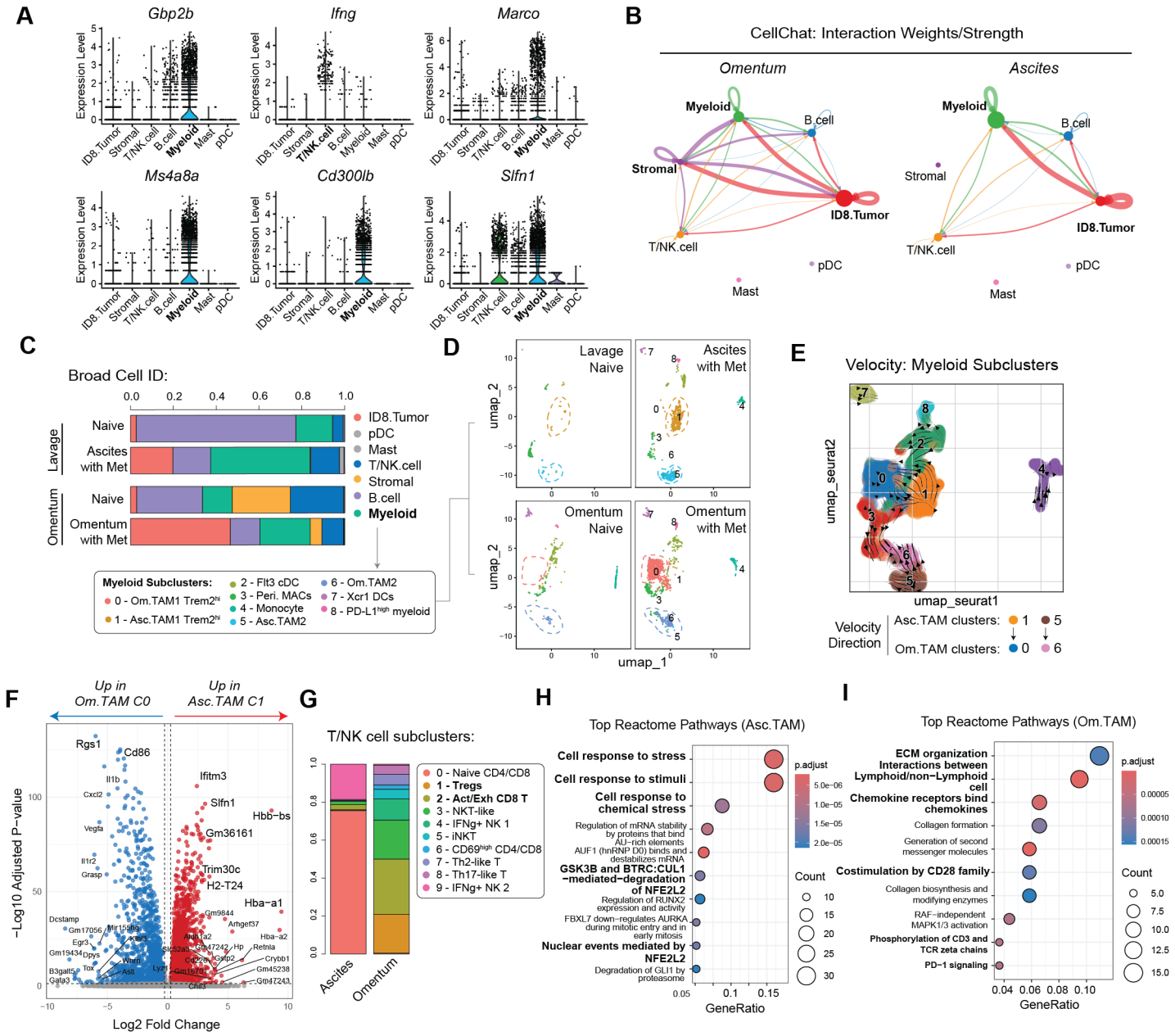

Figure 5: Niche-specific Transcriptional States of Omental and Ascites-Derived TAMs
(**A**) Violin plots depicting CRISPR screen hits expression level across Broad cell ID categories (cell types). (**B**) CellChat-generated circus plots of interaction strengths between Broad cell ID categories in metastatic omentums (left) and ascites (right). (**C**) Stacked bar chart of cell type proportions across the four experimental groups. (**D**) UMAPs of reclustered myeloid cells, split by experimental condition. (**E**) UMAP of subclustered myeloid cells overlayed with scVelo RNA velocity arrows. Arrows are pointing from ascites TAMs (clusters 1 and 5) to omentum TAMs (clusters 0 and 6). (**F**) DEG volcano plot comparing gene expression differences between ascites TAM cluster 1 and omentum TAM cluster 0. (**G**) Stacked bar chart of subsetted T/NK cells comparing cell proportions in ascites and omentum. (**H-I**) Dot plots depicting Reactome pathways enriched in ascital (H) and omentum-derived TAMs (I). Significance of DEGs in Figure 5F was evaluated by applying the FindMarkers() and Wilcoxon test in Seurat to compare ascites and omental Cd68^{high}/Adgre1^{high} macrophages.

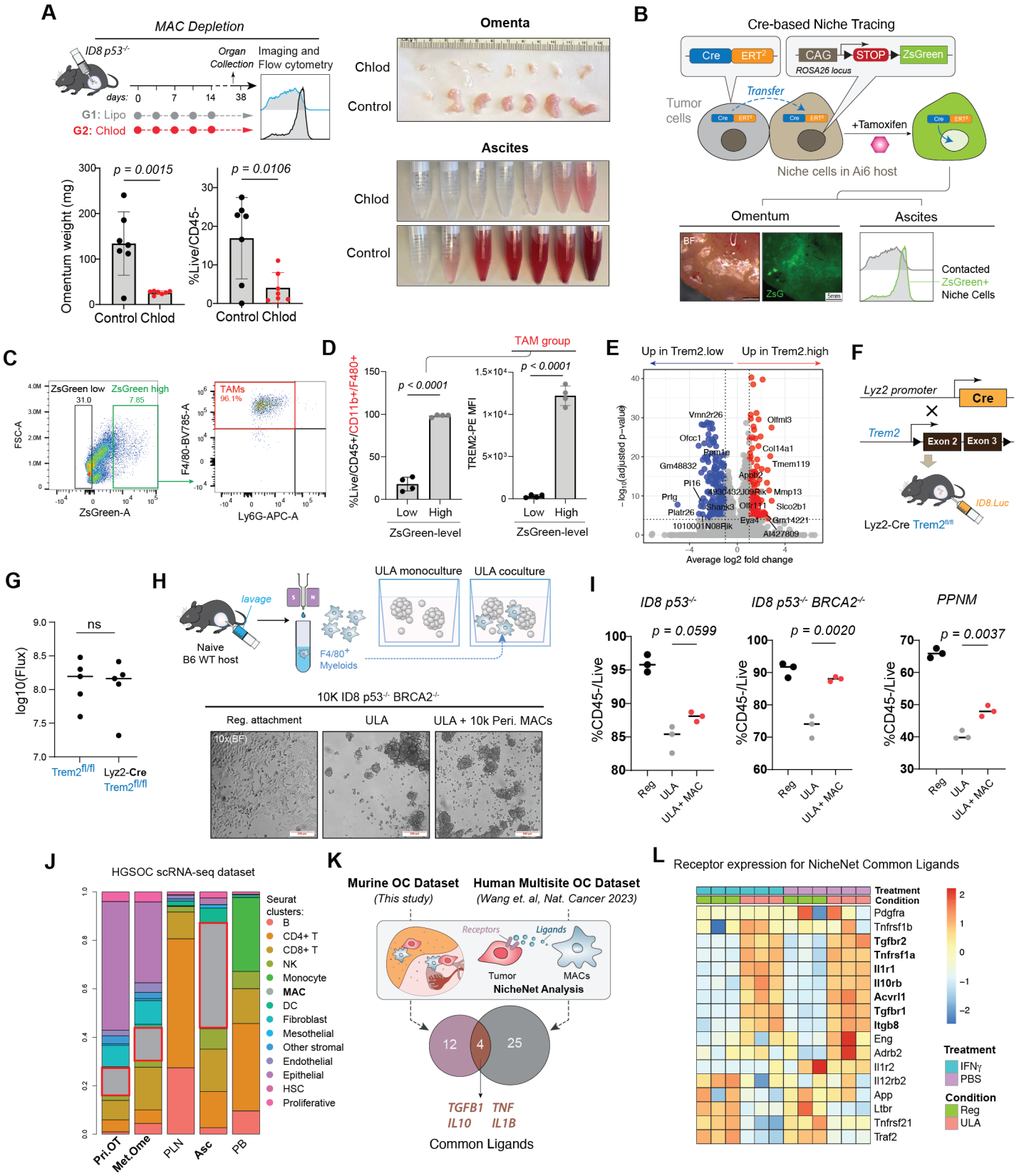
A
MAC Depletion
ID8 p53-/-
Organ Collection
Imaging and Flow cytometry
days: 0 7 14 38
G1: Lipo
G2: Chlod
Omentum weight (mg)
p = 0.0015
Control Chlod
%Live/CD45-
p = 0.0106
Control Chlod
Omenta
Chlod
Control
Ascites
Chlod
Control
B
Cre-based Niche Tracing
Cre ERT2
CAG STOP ZsGreen
ROSA26 locus
Tumor cells
Transfer
+Tamoxifen
Niche cells in Ai6 host
Omentum
Ascites
BF
ZsG
Contacted ZsGreen+ Niche Cells
C
ZsGreen low ZsGreen high
31.0
7.85
FSC-A
ZsGreen-A
TAMs
96.1%
F4/80-BV785-A
Ly6G-APC-A
D
TAM group
%Live/CD45+/CD11b+/F480+
p < 0.0001
Low High
ZsGreen-level
TREM2-PE MFI
p < 0.0001
Low High
ZsGreen-level
E
Up in Trem2.low
Up in Trem2.high
Vmn2r26
Ofcc1
Ppm1e
Gm48832
Pi16
Prtg
Platr26
1010001N08Rik
4930432J09Rik
Shank3
Olfml3
Col14a1
Tmem119
Apbb2
Mmp13
Olfr1171
Slco2b1
Eya4
Gm14221
AI427809
Average log2 fold change
F
Lyz2 promoter
Cre
Trem2
Exon 2
Exon 3
ID8.Luc
Lyz2-Cre Trem2fl/fl
G
ns
log10(Flux)
Trem2fl/fl
Lyz2-Cre Trem2fl/fl
H
lavage
Naive B6 WT host
F4/80+ Myeloids
ULA monoculture
ULA coculture
10K ID8 p53-/- BRCA2-/-
Reg. attachment
ULA
ULA + 10k Peri. MACs
10x(BF)
I
ID8 p53-/-
p = 0.0599
ID8 p53-/- BRCA2-/-
p = 0.0020
PPNM
p = 0.0037
%CD45-/Live
Reg
ULA
ULA+ MAC
J
HGSOC scRNA-seq dataset
Seurat clusters:
B
CD4+ T
CD8+ T
NK
Monocyte
MAC
DC
Fibroblast
Mesothelial
Other stromal
Endothelial
Epithelial
HSC
Proliferative
Pri.OT
Met.Ome
PLN
Asc
PB
K
Murine OC Dataset
(This study)
Human Multisite OC Dataset
(Wang et. al, Nat. Cancer 2023)
Receptors
Ligands
Tumor
MACs
NicheNet Analysis
12
4
25
TGFB1 TNF
IL10 IL1B
Common Ligands
L
Receptor expression for NicheNet Common Ligands
Treatment
Condition
Pdgfra
Tnfrsf1b
Tgfbr2
Tnfrsf1a
Il1r1
Il10rb
Acvrl1
Tgfbr1
Itgb8
Eng
Adrb2
Il1r2
Il12rb2
App
Ltbr
Tnfrsf21
Traf2
Treatment
IFNγ
PBS
Condition
Reg
ULA

Figure 6: Peritoneal Macrophages are Direct DTC Pro-Survival Interactors

(**A**) Liposomal chlodronate-based macrophage depletion strategy and timeline schematic with representative tissue images. Omental tumor burden quantification and flow-based ascites quantification (bottom). Control group; n= 7, and Chlodrosome; n = 7. (**B**) Schematic describing Cre-based NicheTracing labeling system where ID8 and E0771 cancer cells express Cre.ERT2. Upon nuclear entry of Cre.ERT2 into Ai6 reporter niche cells, labeled niche cells turn ZsGreen positive. (**C**) Representative gating strategy depicting the major cell population tagged with zsG. (**D**) Quantification of F4/80+ and TREM2 mean fluorescent intensity (MFI) of contacted, ZsGreen high cells. (**E**) Volcano plot comparing DEGs between metastasis-infiltrating Trem2-low and Trem2-high macrophages. (**F**) Schematic depicting mouse model for macrophage-specific Trem2 knockout. (**G**) Log transformed BLI-derived flux values in Trem2$^{fl/fl}$ (wild type; n = 5) and Lys2-Cre/Trem2$^{fl/fl}$ (knockout; n = 5) mice at metastasis endpoint. Mice were injected with ID8 p53-/- Luciferase cells. (**H**) Schematic of macrophage-cancer cell coculture layout (top) and representative coculture images for one cell line (bottom).(**I**) Plots of percent CD45 negative cancer cell viability (ZombieAqua negative) post coculture in three cell lines. (**J**) Stacked bar chart of main cell type proportions captured in human scRNA-seq dataset across five anatomical locations, using maintype-2 annotation provided by publisher. (**K**) Venn diagram of top NicheNet predicted ligands after filtering for robust expression and overlapping with top ligands in our murine dataset. (**L**) Heatmap comparing enrichment of a curated list of receptors in bulk RNA-seq comparing ULA-cultured cells treated with IFNγ and regular attachment conditions. Data in Figures 6D was plotted as mean with SD and differences between groups were compared via a two-tailed unpaired Student's t test. Data in Figures 6I was similarly analyzed using a Student's t test and plotted with median values. Data in Figure 6E was analyzed using the FindMarkers() function in Seurat and Wilcoxon test to compare gated Trem2-low and Trem2-high cells. RNA-seq heatmap data in 6L was analyzed using DESeq2 and visualized as variance-stabilized counts.